

2018-01-01

# Implementation of Magnesium Alloy AZ91D on Wire and Arc Additive Manufacturing

David Adrian Martinez Holguin

*University of Texas at El Paso*, davidmts@live.com.mx

Follow this and additional works at: [https://digitalcommons.utep.edu/open\\_etd](https://digitalcommons.utep.edu/open_etd)



Part of the [Biomedical Commons](#), [Materials Science and Engineering Commons](#), and the [Mechanics of Materials Commons](#)

---

## Recommended Citation

Martinez Holguin, David Adrian, "Implementation of Magnesium Alloy AZ91D on Wire and Arc Additive Manufacturing" (2018). *Open Access Theses & Dissertations*. 1480.  
[https://digitalcommons.utep.edu/open\\_etd/1480](https://digitalcommons.utep.edu/open_etd/1480)

This is brought to you for free and open access by DigitalCommons@UTEP. It has been accepted for inclusion in Open Access Theses & Dissertations by an authorized administrator of DigitalCommons@UTEP. For more information, please contact [lweber@utep.edu](mailto:lweber@utep.edu).

IMPLEMENTATION OF MAGNESIUM ALLOY AZ91D ON WIRE  
AND ARC ADDITIVE MANUFACTURING

DAVID ADRIAN MARTINEZ HOLGUIN

Master's Program in Metallurgical and Materials Engineering

APPROVED:

---

Namsoo Kim, Ph.D., Chair

---

Guikuan Yue, Ph.D.

---

Jong Wha Chang, Ph.D.

---

Charles Ambler, Ph.D.  
Dean of the Graduate School

Copyright ©

by

David Adrian Martinez Holguin

2018

## **Dedication**

To my beloved parents, Adrian and Luz Maria, whose effort and sacrifice have made possible the completion of my dreams. My eternal love and gratitude.



IMPLEMENTATION OF MAGNESIUM ALLOY AZ91D ON WIRE  
AND ARC ADDITIVE MANUFACTURING

by

DAVID ADRIAN MARTINEZ HOLGUIN, BS

THESIS

Presented to the Faculty of the Graduate School of

The University of Texas at El Paso

in Partial Fulfillment

of the Requirements

for the Degree of

MASTER OF SCIENCE

Department of Metallurgical, Materials, and Biomedical Engineering

THE UNIVERSITY OF TEXAS AT EL PASO

May 2018

## **Acknowledgements**

This work was supported by the Korean Institute of Machinery & Materials (KIMM), (project 226-9003-06A.).

I would like to thank Dr. Namsoo “Peter” Kim, my advisor, for his unconditional support in this project. Also, I would also thank my advisors Dr. Guikuan Yue and Dr. Jong Wha Chang, for their thoughtful comments during the process of completing of this thesis.

I would like to acknowledge all the work done by Dr. Monica Michel. Her support in the process of purchase of materials, design of the experiment, characterization and analysis of results, among many other tasks, significantly helped me in the completion of this project.

## **Abstract**

As progress on Additive Manufacturing (AM) techniques focusing on ceramics and polymers evolve, metals continue to be a challenging material to manipulate when fabricating products. Current methods, such as Selective Laser Sintering (SLS) and Electron Beam Melting (EBM) face many intrinsic limitations due to the nature of their processes. Material selection, elevated cost and low deposition rates are some of the barriers to consider when one of these methods is to be used for the fabrication of engineering products. The research here presented demonstrates the use of a Wire and Arc Additive Manufacturing (WAAM) system for the creation of metallic specimens. This project explored the feasibility of fabricating elements made out of Magnesium alloys with the potential to be used in biomedical applications. It is known that the elastic modulus of magnesium (41-45 GPa) is more similar of that of natural bone (3-20 GPa) comparing with other metals. Thus, stress shielding phenomena can be reduced. Furthermore, the decomposition of Magnesium represents no harm inside the human body, since it is an essential element in the body and its decomposition products can be easily excreted through the urine. By alloying magnesium with aluminum and zinc, or rare earths such as Yttrium, Neodymium, Cerium, and Dysprosium the structural integrity of specimens inside the human body can be assured. However, the in-vivo corrosion rates of these products can be accelerated by the presence of impurities, voids, or segregation created during the manufacturing process. Fast corrosion rates would produce improper healing, which, in turn, involves subsequent surgical intervention. Magnesium alloy AZ91D based lines has been produced using the WAAM described in this research. Specimens created under different condition have been analyzed macro and microscopically in order to determine those parameters that yield visual and microstructural results.

## Table of Contents

Acknowledgements .....	v
Abstract.....	vi
Table of Contents.....	vii
List of Tables .....	ix
List of Figures.....	x
List of Illustrations.....	xiii
Chapter 1: Additive Manufacturing.....	1
1.1 Selective Laser Sintering (SLS) .....	2
1.2 Electron Beam Melting.....	4
1.3: Limitations of Additive Manufacturing Techniques for the Fabrication of Metallic Components .....	6
1.3.1 Feedstock .....	7
1.3.2 Energy Consumption .....	8
1.3.3 Health and Safety Hazards .....	8
1.3.4 Structural Integrity.....	8
Chapter 2: Wire and Arc Additive Manufacturing (WAAM) .....	11
2.1 Selection of Filler Materials .....	12
2.2 Investment .....	12
2.3 Workspace .....	13
Chapter 3: Magnesium as Biomaterial .....	14
3.1 Magnesium for Biomedical Applications.....	15
3.2 Magnesium Welding.....	17
Chapter 4: Preliminary work .....	18
4.1 Creation of the System .....	18
4.2 Selection of Power Supply and Heat Source .....	26
4.3 Gas-Tungsten Arc Welding (GTAW) .....	27
4.3.1 Direct-Current Electrode Negative (DCEN) .....	27
4.3.2 Direct Current Electrode Positive (DCEP) .....	27

4.4 Plasma Arc Welding (PAW) .....	30
4.5 System Functioning .....	32
Chapter 5: Experimental Procedure .....	34
5.1 Materials .....	34
5.1.1 Magnesium Alloy AZ91D. ....	34
5.1.2 Stainless Steel 316 .....	36
5.2 Determination of Optimal Printing Parameters .....	39
5.3 Analysis and Characterization .....	41
5.3.1 Optical Microscopy .....	41
5.3.2 X-Ray Diffractometry .....	43
5.3.3 Scanning Electron Microscopy .....	43
5.3.4 Electron-Dispersive Spectrometer .....	45
Chapter 6: Results .....	46
6.1: Characterization of As-Received AZ91D Wire .....	46
6.2: Macroscopical Features .....	47
6.3: Macroscopical Analysis .....	53
6.4: Diffractometry and Spectrometry .....	57
6.5: Characterization of By-products .....	60
Chapter 7: Discussion .....	62
7.1: On Macroscopical Appearance .....	62
7.2: On Contact Angle .....	63
7.3: On Microstructural Changes .....	67
References .....	70
Vita	74

## List of Tables

Table 2.1: Comparison of static properties of typical wrought, EOS M280, ARCAM A2 and WAAM processed Ti-6Al-4V. Data retrieved from[1] .....	11
Table 3.1: Summary of the physical and mechanical properties of various biocompatible metals in comparison to natural bone [28]. .....	15
Table 5.1: Chemical composition of magnesium alloy AZ91D[42]. .....	35
Table 5.2 Physical properties of magnesium alloy AZ91D[42]. .....	35
Table 5.3: Mechanical properties of magnesium alloy AZ91D[42]. .....	35
Table 5.4: Chemical composition of Stainless Steel 316[44]. .....	37
Table 5.5 Physical properties of Stainless Steel 316[44]. .....	38
Table 5.6: Mechanical properties of Stainless Steel 316[44]. .....	38
Table 6.1: Average width and standard deviation of printed lines under all the printing parameters.....	51
Table 6.2: Average height and standard deviation of printed lines under all the printing parameters.....	51
Table 6.3: Standard deviation of the width of the lines as a function of the arc current. ....	52
Table 6.4: Standard deviation of the height of the lines as a function of the arc current. ....	52
Table 6.5: Standard deviation of the width of the lines as a function of the printing speed. ....	52
Table 6.6: Standard deviation of the height of the lines as a function of the printing speed. ....	53
Table 7.1: Heat input depending on printing conditions. ....	66

## List of Figures

Figure 1.1: Complex structure created with the use of Electron Beam Melting (EBM) additive manufacturing[3] .....	1
Figure 1.2: Schematic functioning of an Electron Beam Melting (EBM) system [12].....	5
Figure 1.3: Comparison between products fabricated using CNC systems (left) and AM techniques (right). Structure on the left-hand side made out of aluminum, while the sample on the right is a polymer. Function of the product not specified [15]. ....	6
Figure 1.5: Detailed image of non-molten steel particles bounded in molten copper, surrounded by voids (black regions)[23]. .....	9
Figure 1.6: View of several laser sintering tracks (brighter regions). Voids present in the sections where the laser did not pass through[23]. .....	10
Figure 2.1: 10-meter (32.8-ft) Wire + Arc Additive Manufacture (WAAM) metals 3D printer. Motion Control provided by robotic [24]. .....	13
Figure 3.1: The use of Tungsten-arc Inert Gas welding for magnesium welding[43]. ....	17
Figure 4.1: First version of the motion system created. X-Y axes controlled by aluminum frame lying on a flat surface. Z axis movement system fixed to the wall. Heat source (plasma torch) and wire feeder (5V stepper motor) fixed on the pedestal. ....	20
Figure 4.2: Modifications required for the use of filler wire of OD>1mm. “Wire Feeder” being the original 5V stepper motor, while “Secondary Extruder” refers to the 12V motor. ....	21
Figure 4.3: Couple formed by the CPU (Arduino Mega 2650, blue board on bottom) and “shield” board (RAMPS 1.4). .....	23
Figure 4.4: X-Y motion control with water cooling system. ....	24
Figure 4.5: Incorporation of a heating element to reduce the temperature differential. The element was placed on top of a ceramic plate to avoid heat induced damage to the moving system. ....	25

Figure 4.6: Pro-Fusion Dual Arc 82HFP welding machine used a power supply .....	26
Figure 4.7: Comparison between Gas-Tungsten arc (Left) and Plasma arc (right) [48]. .....	32
Figure 5.1: Change in microstructure as a function of the alloying content[54]. .....	37
Figure 5.2: Visual representation of the selection of printing parameters. ....	40
Figure 5.3: KEYENCE VHX-900 Digital Microscope equipped with a VH-Z100UR lens used for optical microscopy .....	42
Figure 5.5: Example of Hitachi S4800 SEM equipped with EDAX EDS system. ....	45
Figure 6.1: Optical micrograph of a longitudinal cot of the as-received AZ91D wire. 1000X. Etched with glycol. ....	46
Figure 6.2: XRD spectra of as-received wire. Representative peaks of magnesium ( $\alpha$ phase), zinc, and $Mg_{17}Al_{12}$ precipitates ( $\beta$ phase). ....	47
Figure 6.3: Visual representation of the macroscopical appearance of printed lines created under different printing conditions. ....	48
Figure 6.4: Increase in the temperature of the printing plate under two different printing conditions (lowest and highest heat input) as the number of lines printed increases. Critical temperature for detachment shown by dashed lines. ....	50
Figure 6.5: Sequence of steps for the detachment of lines from printing plate. I)Firmly hold the line with pliers. II) Twist the printed line to break the temporary bond. III) Separate the line from the substrate. ....	50
Figure 6.6: Representative microstructure of printed lines. $Al_{15}Mg_{11}Zn_4$ precipitate ( $\phi$ phase) embedded on a Mg matrix ( $\alpha$ phase). 1000X. Glycol as etchant. ....	54
Figure 6.7: Characteristic defects present on printed lines. A&B show cracks formed at the top section of the samples. C&D presenting cracks growing from the bottom inwards .....	55
Figure 6.8: Decrease on contact angle (Y axis) as consequence of both printing parameters current intensity (X axis) and printing speed (graphed lines). ....	56



Figure 6.9: Micrographs of lines printed consecutively over the same substrate under the same printing conditions. I) First line printed, II) second line printed, and III) third line printed. The decrease in contact angle as the number of lines printed increases is noticeable. ....	56
Figure 6.10: XRD spectra of a representative printed line. Representative peaks of pure magnesium ( $\alpha$ phase) and $\text{Al}_5\text{Mg}_{11}\text{Zn}_4$ precipitates ( $\phi$ phase). ....	57
Illustration 6.1: Diagram representing the areas from which the elemental mappings were gotten. ....	58
Figure 6.11: Elemental Mapping of zone 1. ....	59
Figure 6.12: Elemental Mapping of zone 2. ....	59
Figure 6.13: Different by-products created depending on printing conditions. 6.12A; line printed under low heat conditions presenting black powder. 6.12B; Line printed using higher heat input presenting white a mixture of white and black powder. ....	60
Figure 6.14: XRD spectra of by-products. Pure magnesium (black powder) and magnesium oxide (white powder) were found. ....	61
Figure 7.1: Line printed under conditions of high heat and high speed. A “river-like pattern”, through which the molten metal flowed while dragged along the solidified metal (beginning on the line). ....	63

## List of Illustrations

Illustration 1.1: Basic Functioning of Powder Bed Systems. Source:[1] .....	3
Illustration 1.2: Basic Functioning of Powder Feed Systems. Source:[1] .....	3
Illustration 1.3: Schematic functioning of a Selective Laser Sintering (SLS) system. Source: [6].....	4
Illustration 4.1: Connection diagram of the components used on the controlling couple. ....	22
Illustration 4.2: (a) Schematic of the wiring required for GTAW welding. (b) Schematic of the internal components and functioning of GTAW (TIG) torches [37].....	28
Illustration 4.3: Flow of the current and penetration of the arc as a function of the polarity.....	29
Illustration 4.5: I) Diagram of the functioning of the WAAM system created. II) Relative position of the arc and wire required for good results. ....	33
Illustration 7.1: Forces involved in the determination of the contact angle of a liquid drop over a flat solid surface.....	64

## Chapter 1: Additive Manufacturing

Additive manufacturing (AM) is defined by the American Society for Testing of Materials (ASTM) as “the process of joining materials to make objects from 3D model data, layer upon layer”[1]. AM production methods have been used for rapid prototyping using Computer Assisted Designs (CAD) models. Polymers are the most common material selection due to their low melting point and low production cost. Two main techniques are now used for 3D printing: Stereolithography (STL) and fused deposition modeling (FDM). The evolution of the production techniques has made possible the use of AM structures as final products. In contrast with traditional subtractive fabrication techniques, such as Computer Numerically Controlled (CNC) machining, AM offers many advantages. The complete automatization of the process from a CAD/CAM file can be achieved, saving on production cost[2]. The majority of direct deposition methods have low energy consumption, compared to traditional machining tools. Also, the layer-by-layer structure allows the creation of complicated geometries. Rapid manufacturing methods have become increasingly popular for their overall monetary savings, low environmental impact, and ability to create complex geometries[1].

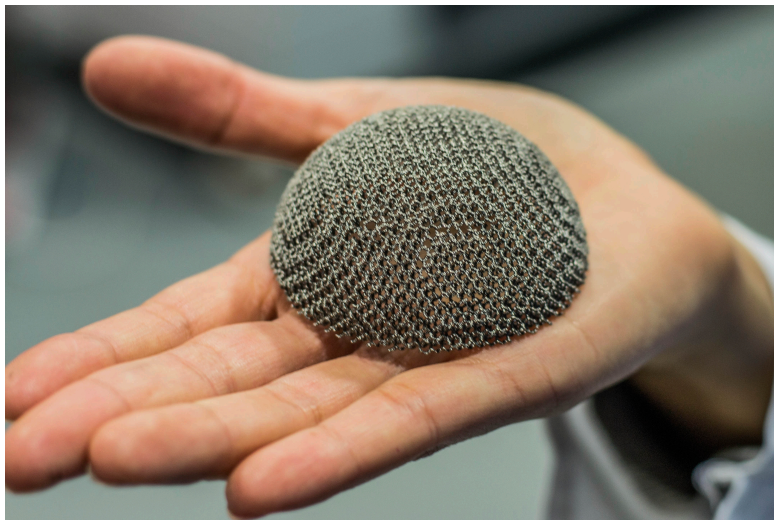


Figure 1.1: Complex structure created with the use of Electron Beam Melting (EBM) additive manufacturing[3]

As progress on methods focusing on ceramics and polymers evolve[4][5][6], metals continue to be a challenging material to manipulate when fabricating products[7]. In order for a metal to be deposited over a printing bed, the molten or semi-molten state must be achieved. In general, metals used for structural purposes have a moderate to high melting point, so high amounts of energy must be introduced to the filler material in order to melt it. During the cooling process, metals undergo continuous cycles of phase changes which alter the microstructure and, ultimately, the mechanical properties of the final product. Traditional metal printing use metal powders as filler material, which can be either fed or sparse on the bed, and a heat source (high energy electron beam or a high frequency laser). Powder Bed (PBAM) and Powder Feed (PFAM) are two categories that distinguish the equipment used to fashion parts from AM-grade powdered metal. In PBAM a fine layer of metallic powder is loosely dispersed over the whole printing area before the printing of each layer (Illustration 1.1). On the other hand, PFAM relies on the continuous feeding of powder directly under the heat source (Illustration 1.2). Popular methods that use powdered metal are Selective Laser Sintering (SLS), Selective Laser Melting (SLM), and Electron Beam Melting (EBM)[8]. The heat source in these systems is either an electron beam or a high frequency laser focused on a localized area. However, like with any engineering design, there is room for optimization in areas that have problems.

### **1.1 SELECTIVE LASER SINTERING (SLS)**

Selective Laser Sintering (SLS) uses a carbon dioxide laser beam in order to fuse or sinter metallic powder. In order to do that, the temperature inside the printing chamber has to be increased until it almost reaches the melting temperature of the material. Then, the laser fuses localized sections of the powder bed[9]. The areas in which the laser will sinter the feedstock is specified on the digital design. After one layer of the designed is finished, the bed is lowered with the use of a piston. A new layer of powder is deposited over the previous layer and the process continues[1]. The time needed for an individual particle to get fused to the neighboring one is a function of both the beam size and the scanning speed[9]. SLS can be used not only for

the fabrication of metallic components but also for polymers, ceramics, and combinations of two or more materials to create composites[10][11]. Illustration 1.3 shows a schematic of the functioning of a SLS system.

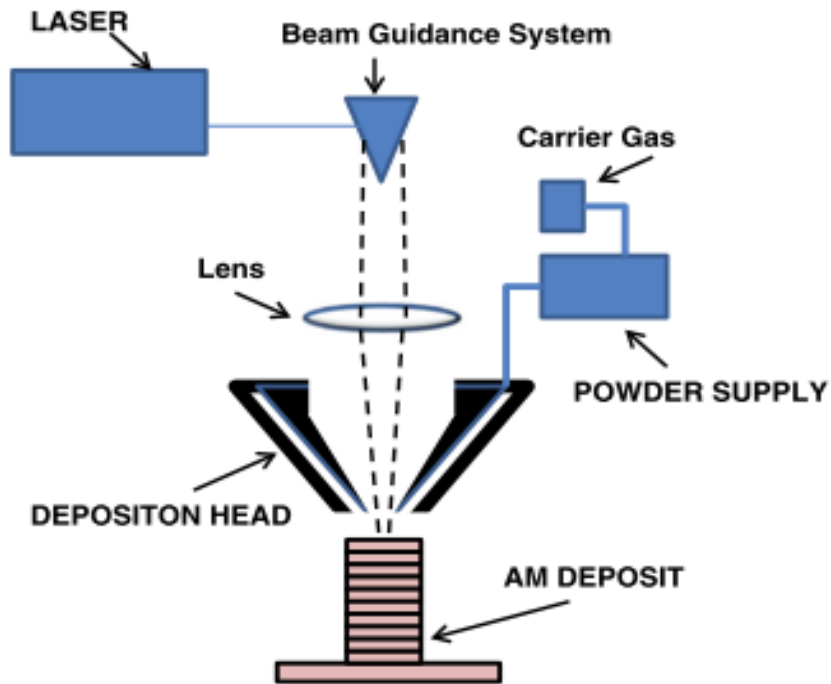


Illustration 1.1: Basic Functioning of Powder Bed Systems [1].

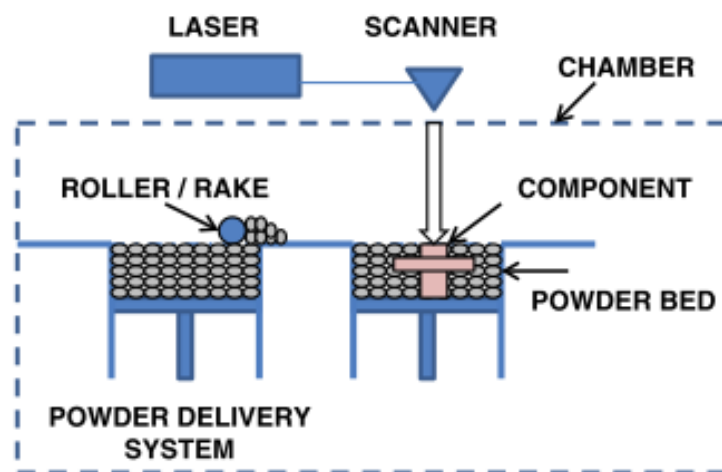


Illustration 1.2: Basic Functioning of Powder Feed Systems [1].

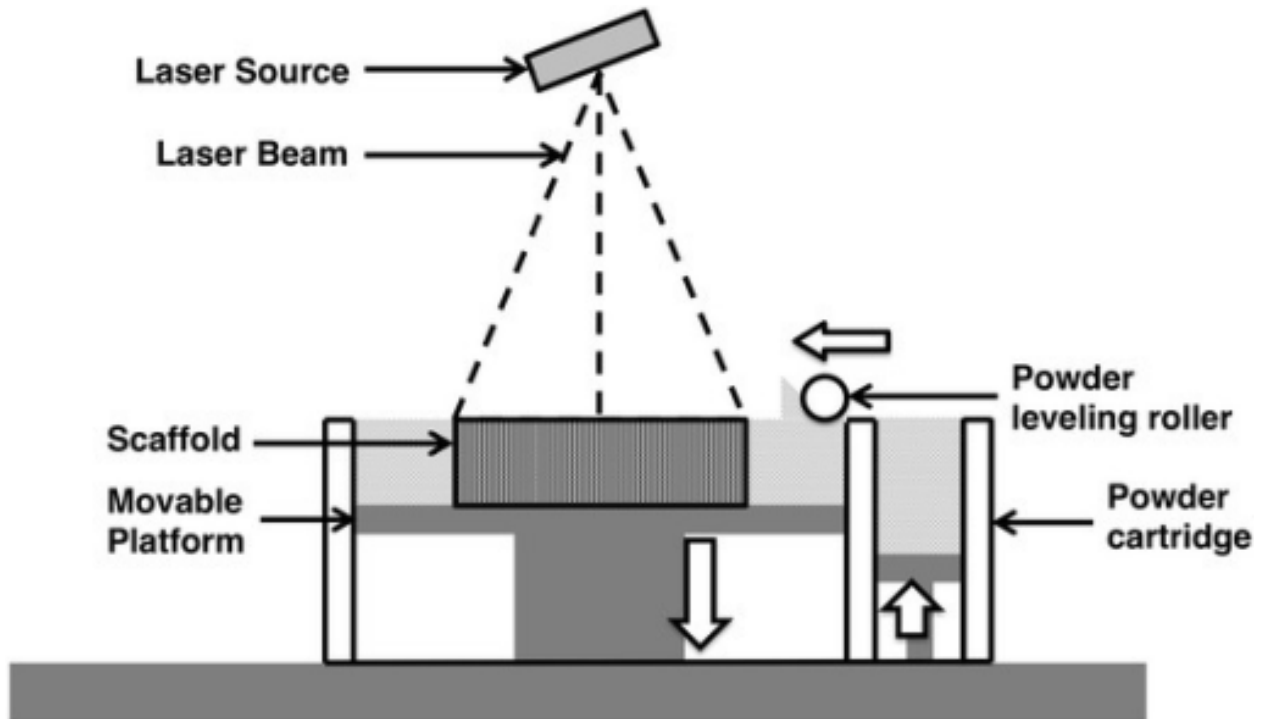


Illustration 1.3: Schematic functioning of a Selective Laser Sintering (SLS) system [11].

## 1.2 ELECTRON BEAM MELTING

Electron Beam Melting process is much similar to SLS techniques. In this new method, however, a high voltage electron laser beam melts the metallic powder. The typical acceleration voltage ranges from 30 to 60 KV[10]. Since EBM is designed for the fabrication of metallic components, a high vacuum has to be created in the printing chamber in order to avoid oxidation problems[12]. In a similar manner than SLS, pre-alloy metallic powders are used instead of a controlled mixture of different pure metals in order to avoid segregation issues. Since the workspace requires high vacuum, the use of EBM is projected for its use in outer space[13]. Figure 1.2 shows functioning of an EBM additive manufacturing system.

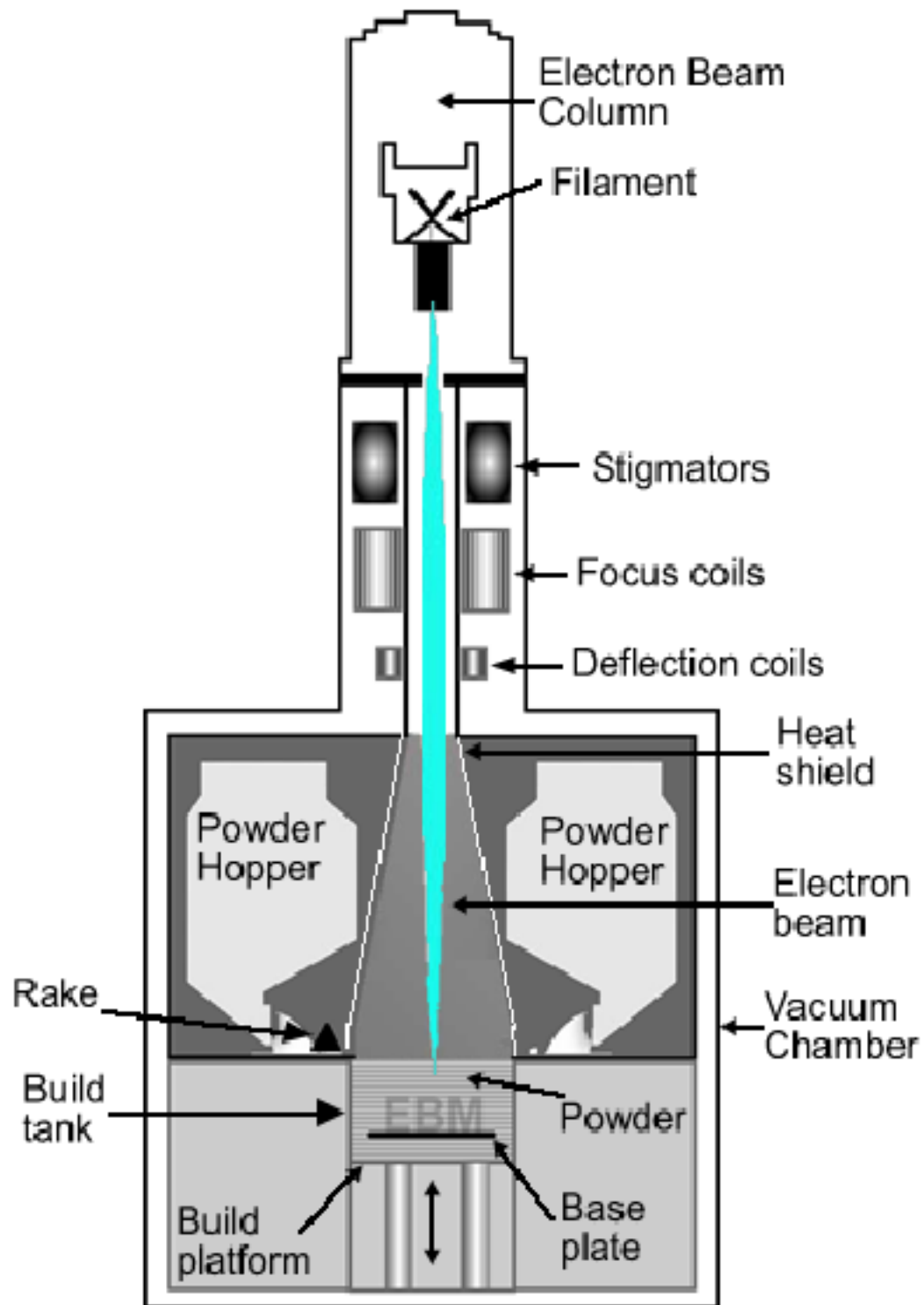


Figure 1.2: Schematic functioning of an Electron Beam Melting (EBM) system [12].

### 1.3: LIMITATIONS OF ADDITIVE MANUFACTURING TECHNIQUES FOR THE FABRICATION OF METALLIC COMPONENTS

SLS and EBM additive manufacturing has become in the last decade the most widely accepted Rapid Prototyping (RP) techniques. Improvements in the methodologies of both processes have increased the quality of the products fabricated with them. However, in order for them to become large scale production techniques some conditions have to be fulfilled. Consistency in the mechanical properties, as well as in the visual quality of the final products has to be ensured. Complex geometry, such as overhanging surfaces and internal structures are hard to manufacture with the use of AM techniques, which are relatively simple tasks for extractive manufacturing (CNC systems). Most importantly, the breakthrough of AM processes into the large scale industry will depend on reliability, performance and economic aspects, such as the case of production time and cost[14]. A comparison between products fabricated using CNC and AM systems is shown in Figure 1.3. Intrinsic limitations have hindered the full implementation of AM techniques on the industry. Some examples of these obstacles are discussed below.

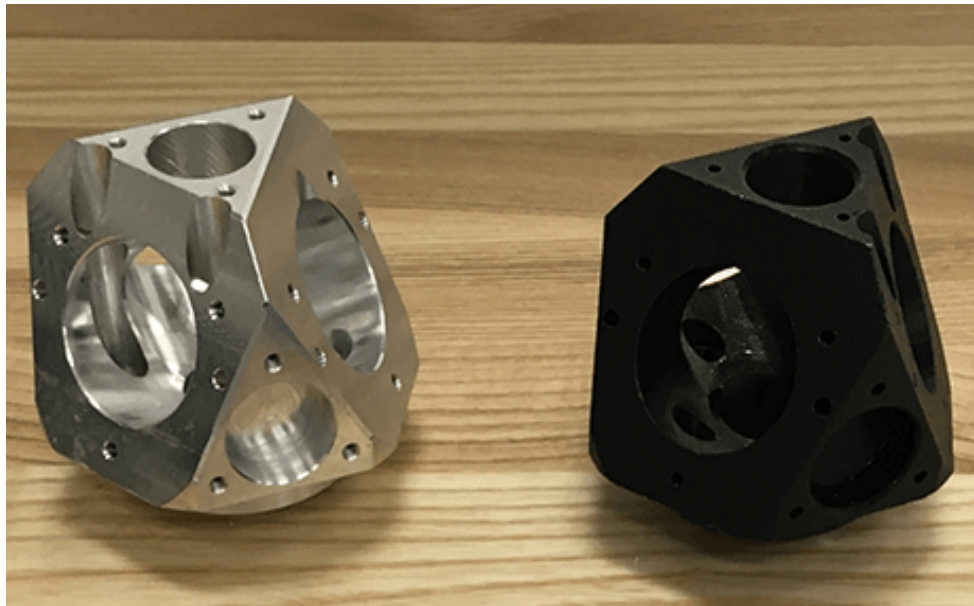


Figure 1.3: Comparison between products fabricated using CNC systems (left) and AM techniques (right). Structure on the left-hand side made out of aluminum, while the sample on the right is a polymer. Function of the product not specified [15].



### 1.3.1 Feedstock

PBAM and PFAM systems rely on the use of metal powder as feedstock. The processing of pure metals or metal alloys is generally an expensive process. A dramatic increase in the total surface area of the metals can be observed when they are processed as powders. Thus, phenomena such as oxidation can be easily found when dealing with small size particles. In order to maintain the chemical and structural integrity of the powders, special handling and storing techniques must be adopted[16]. A good distribution in the shape and size of the particles must be achieved to ensure a proper density on the final products. It has been found that adding 30% of fine particles, having a size ratio of 1:7, increases the density of the powder bulk by about 30%, which, in turn, will increase the density of the final product in the same proportion[17], [18]. Figure 1.4 shows an SEM image of nickel powder used for SLS. It is observable that different particle sizes were used in order to decrease the free-space volume.

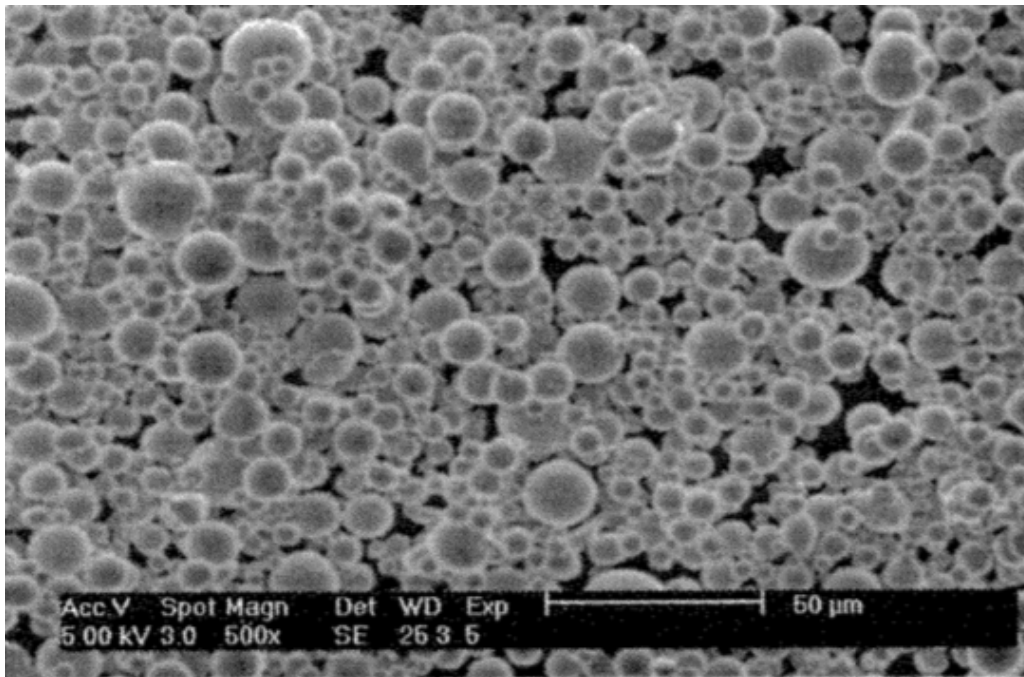


Figure 1.4: SEM image of nickel powder used on SLS systems [17].

### ***1.3.2 Energy Consumption***

As mentioned before, SLS and EBM techniques rely either on a high energy laser or an electron beam for the creation of 3D structures. Both cases required large amounts of energy for the creation of these heat sources. The creation of a localized atmosphere is also required for powder bed and powder feed systems. In laser sintering techniques the temperature of the chamber has to be increased to almost the melting temperature of the material which is being printed. Inconel 718 is one of the most widely materials used in the Aerospace industry. Due to its excellent mechanical properties and structural and chemical stability at elevated temperatures ( $>700^{\circ}\text{C}$ ) it is suitable for application in gas turbine blades, corrosion containments, turbocharger rotors, among many others[19]. Having a melting temperature of  $1210^{\circ}\text{C}$  - $1344^{\circ}\text{C}$ , when fabricated using SLS the chamber temperature cannot be lower than  $1000^{\circ}\text{C}$ [19]. In order to achieve these temperatures, a large consumption of energy is required. In the case of EBM, the necessity of a high vacuum also affects the required energy input.

### ***1.3.3 Health and Safety Hazards***

Safety and health of the operators must be the number one priority in every manufacturing facility. In order to protect the human life standards and laws have been set by those patrolling the industry. As AM becomes more prevalent throughout production facilities, unknown safety risks may arise. One danger when using powder feed AM is the high risk of inhalation. Foreign materials may enter the body through orifices, such as the mouth, eyes or nose, and this can lead to intoxication. Since the human body cannot get rid of the metals, hazardous levels can be achieved quickly, and health problems may develop[20].

### ***1.3.4 Structural Integrity***

Due to its intrinsic functioning, SLS present manufacturing issues such as lack of fusion and micro-porosity. Since the molten state is not necessarily achieved, the fusion between neighboring particles is not completely ensured. The dispersion of metal powder restricts the heat

transfer and complicates the fusion across particle boundaries. The presence of oxide layers on the metallic powder can also lead to lack of fusion[21]. Micro-porosity can arise from two sources; a deficient distribution in the size and shape of the particles forming the metallic powder that leads to the presence of a high amount of empty space between the neighboring particles, and humidity present in the powder that can form water vapor pockets within the final product[22]. A combination of porosity and deficient sintering can be seen in Figure 1.5. The presence of these kind of defects can lead to decreased mechanical properties and higher corrosion rates[13]. Moreover, different raster patterns (direction in which the laser or electron beam moved for the creation of the structure) may result in different mechanical responses in different directions (anisotropy)[23]. The raster pattern is easily observed on Figure 1.6.

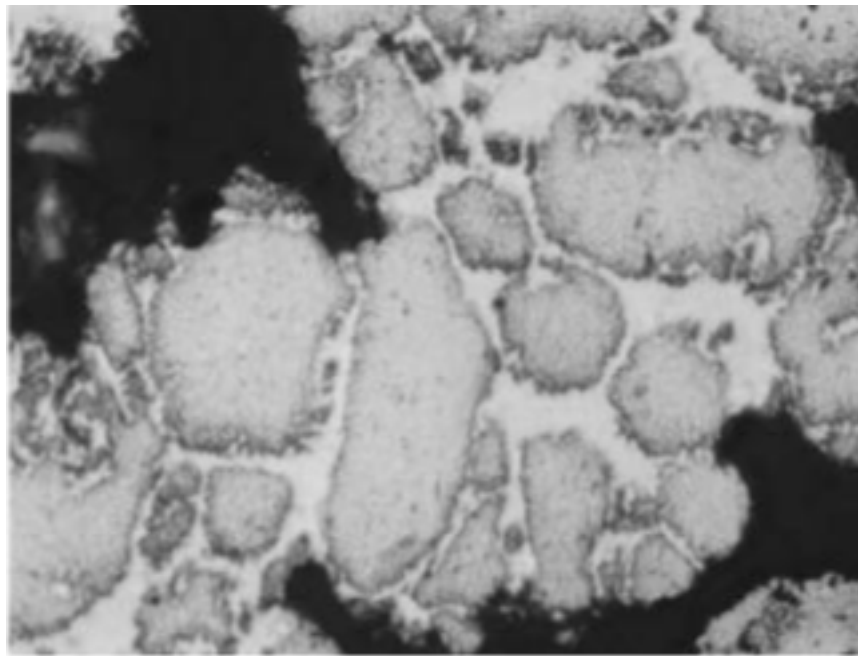


Figure 1.5: Detailed image of non-molten steel particles bounded in molten copper, surrounded by voids (black regions)[23].

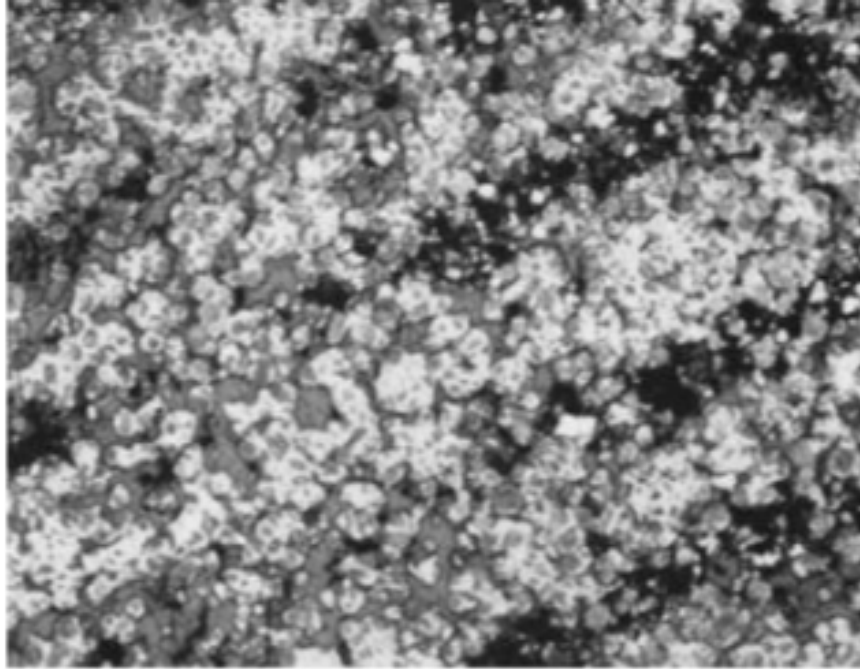


Figure 1.6: View of several laser sintering tracks (brighter regions). Voids present in the sections where the laser did not pass through[23].

## Chapter 2: Wire and Arc Additive Manufacturing (WAAM)

Wire and Arc Additive Manufacturing combines an electric arc (heat source) and a metal wire as feedstock in order to create 3D models in a bottom up approach (layer upon layer) [1]. Even though the first patent for these type of systems was filed on 1925, it was until the 1990s when WAAM started being investigated as an AM technique [24]. The equipment required for the creation of WAAM systems can be easily bought on hardware stores, since these techniques relies on the use of off the shelf welding equipment. Welding power sources, torches, and wire feeding systems are some of the pieces that can be borrowed from welding equipment [24]. CNC or robotic systems can be used to provide the required movement. Due to its simplified design and the feedstock, WAAM present many advantages over powder bed and powder feed systems. Recent studies have demonstrated that mechanical properties of Ti-6Al-4V, such as yield strength and ultimate tensile strength (UTS), in directions parallel to the layers are superior for specimens manufactured using WAAM than those of products created by SLS (EOS M280 system), EBM (ARCAM A2 system), and that typical wrought processes [1]. Comparison of mechanical properties in X-Y and Z directions are even shown in Table 2.1. The following points are the most important reasons why this technique was adopted for this project.

Table 2.1: Comparison of static properties of typical wrought, EOS M280, ARCAM A2 and WAAM processed Ti-6Al-4V [1].

<i>Property-Direction</i>	<i>Typical Wrought</i>	<i>EOS M208</i>	<i>ARCAM A2</i>	<i>WAAM</i>
<i>YS, X-Y (MPa)</i>	828	887	848	950
<i>YS, Z (MPa)</i>	828	949	841	803
<i>UTS, X-Y (MPa)</i>	897	997	946	1033
<i>UTS, Z (MPa)</i>	897	1010	946	918

## **2.1 SELECTION OF FILLER MATERIALS**

The use of a solid material (wire) rather than powders allows the use of wider material selection. Wire is formed by casting a billet, sectioning it, undergoing drawing, which results in subjecting it to continuous tensile forces, pushing through a gauge to obtain a desired cross-sectional area [25]. When extruded at high temperatures ( $>0.6T_M$ ) brittle materials, such as magnesium alloys, can be drawn to small diameters ( $<1\text{mm}$ ) [26]. Dedicated handling and storing techniques are not as strictly necessary when manipulating solid metals. The use of wire also reduces the risk of violent reaction than can arise from the use of metallic power, since the reduction in surface area also decreases the reactivity of the metal[27]. Health hazards are also reduced since the handling of powders is eliminated.

## **2.2 INVESTMENT**

While powder bed or powder feed systems would represent a monetary investment of more than U\$200,000, WAAM systems can be easily assembled with no more than half of that amount. If a complex equipment is to be created, a six-axis robot can be used, which would represent an investment of approximately U\$50K. Regarding the power source and heat supplier, the investment would be not be superior of U\$30K[24]. Of course, the price of these components can vary dependent on the characteristics of each one of them. Filler material would also represent decrease in the capital investment. Generally, a metal processed as wire can be found at lower prices than its powdered version. Energetic consumption is also reduced when comparing powder-based systems and WAAM. By eliminating the necessity of creating an electron beam or a high frequency laser the required electrical input is lowered. In contrast to EBM techniques, that use accelerating voltages from 30 to 60 kV[10], Plasma Arc Welding (PAW) systems can be used on 110V configurations. Powdered metal is made up of individual morphed spheres in different sizes. This dispersion of metal, restricts the heat transfer and complicates the fusion across particle boundaries. Due to the lack of continuity in the structure, more heat is required to

commence phase transformation. Thus, less energy is necessary for melting wire metals, making it more energetically efficient[28].

### 2.3 WORKSPACE

When dealing with materials that do not need to be processed inside an inert chamber, such as the case of steel, aluminum, magnesium, among many others, the size of final product will be limited only by reach of the moving system[24]. Due to its large deposition rate, big components can be efficiently fabricated using WAAM. In contrast to Powder Bed or Powder Feed systems that can deposit from 1 g/min to 10 g/min, WAAM allows the deposition of larger amounts of material (300+ g/min) [2]. Larger deposition rates can be achieved; however, the resolution of the final product would be sacrificed. Thus, designs with simple geometry can be fabricated faster than those having more complex morphologies.



Figure 2.1: 10-meter (32.8-ft) Wire + Arc Additive Manufacture (WAAM) metals 3D printer. Motion Control provided by robotic [24].

### **Chapter 3: Magnesium as Biomaterial**

During the past couple of decades, important developments in the use of polymer, polymer matrix composites, and ceramics for its in bone healing applications have been achieved [29], [30]. However, despite these important findings, the use of metallic components continues to be the most popular option for these purposes[31]. Due to their superior mechanical proprieties, metals are the choice over polymers and ceramic for load-bearing applications. High fracture toughness and good mechanical strength, as well as good biocompatibility, are desirable properties at the moment of choosing materials for their use in bone healing. The most widely used metallic biomaterials include, but not limited, titanium alloys, cobalt-chromium alloys, and stainless steel. Table 3.1 shows a comparison of mechanical and physical properties between these materials and natural bone, as well as one of the most widely use ceramic materials for bone healing. It is noticeable that for the metals mentioned above, elastic modulus, compressive yield strength, and fracture toughness, are many times larger than those of natural bone. Due to the large mismatch in elastic moduli, problems related to the stress shielding effect arise. Stress shielding occurs when a foreign element (the bone healing device in this case) absorbs some of the load that the bone would withstand naturally. The reduction in stress leads to a decrease in bone density on the areas close to the metallic component may lead to a deficient healing process[32]. Further limitations arise from the possible liberation of harmful metallic ions inside the organism due to corrosion mechanisms, as well as debris formation due to wear, that lead to inflammation in the areas near the biomedical device [33]. Biocompatible metals use for orthopedic or bone healing purposes are known to be inert inside the human body, meaning that the elements will sit inside the carrier until, upon the fulfillment of their design function, they are removed on a secondary surgical procedure, involving increases on the health care system cost[34].



Table 3.1: Summary of the physical and mechanical properties of various biocompatible metals in comparison to natural bone [35].

<i>Properties</i>	<i>Natural Bone</i>	<i>Ti alloy</i>	<i>Co-Cr Alloy</i>	<i>Stainless Steel</i>	<i>Magnesium</i>
<i>Density (g/cm<sup>3</sup>)</i>	1.8-2.1	4.4-4.5	8.3-9.2	7.9-8.1	1.74-2.0
<i>Elastic Modulus (Gpa)</i>	3-20	110-117	230	189-205	41-45
<i>Compressive strength (Mpa)</i>	130-180	758-1117	450-1000	170-310	64-100
<i>Fracture toughness (MPam<sup>1/2</sup>)</i>	3-6	55-115	N/A	50-200	15-40

### 3.1 MAGNESIUM FOR BIOMEDICAL APPLICATIONS

Magnesium has been studied as an alternative for bone healing purposes due to its mechanical properties and degradability inside the human body. Being lighter than aluminum ( $1.74 \text{ g/cm}^3$  compared to  $2.7 \text{ g/cm}^3$ ), magnesium presents fracture toughness greater than ceramic biomaterials. As shown in Table 3.1, the elastic modulus and yield strength of Magnesium are closer to those of human bone, thus, stress shielding phenomena can be drastically reduced. As a biodegradable metal, magnesium elements will progressively corrode inside the human body upon completed the assigned task (bone healing) until no trace of the original elements is present inside the organism[36]. The body requires magnesium ions for both metabolic reactions and biological mechanism. Typically, a 70 Kg person would have approximately 35 g of magnesium[37]. Excess magnesium ions are excreted through the urine with no harm on the metabolic system [38].

The earliest documented attempt of using magnesium-based materials as biomaterial took place on 1907. Albin Lambotte utilized a plate of pure magnesium and steel nails coated with gold to fix the lower bones of a fractured leg. The early attempt failed since the pure magnesium plate dissolved by the eighth day after surgery. It was observed by Lambotte that a large amount of gas evolved under the skin in the area where the plate was placed. Many years after this first

attempt, it was discovered that hydrogen evolves during the corrosion process. Attempts for reducing the corrosion rate took place in more recent years. In 1944, Trioitskii and Tsitron alloyed pure magnesium with small amounts of cerium. Only 9 cases out of the 34 failed, mainly due to infections or difficulties others than the corrosion of the material. Trioitskii and Tsitron reported that the mechanical integrity of the elements was maintained for 6-8 weeks, while traces of the components were not found at 8 months after the procedure. More recently, McBride reported that 1 gram of an Mg-Al-Mn alloy would completely dissolve in 120 days within the human body [36].

The biggest impediment for the use of this metal as screws or plates in bone healing is the high corrosion rate that it presents in aqueous environments, which does not allow the growth of new bone tissue [38]. Magnesium starts corroding in solutions with pH lower than 11.5. Thus, by placing the specimens in vivo, accelerated corrosion is expected (pH equals 7.4 or lower due to secondary acidosis arisen from the surgical process). Furthermore, the high amount of impurities and pores contained in cast structures increase the corrosion rate of the specimens. Due to the low machinability of Magnesium, casting is, to date, the best fabrication method for this element. Intrinsic conditions on this processing technique involve segregation of alloying elements or second phase particles and porosity due to trapped gasses. Both problems will increase the corrosion rate of the produced component.

In this study, the authors explore the implementation of the Wire and Arc Additive Manufacturing (WAAM) technique for the fabrication of impurity-free and void-free elements using AZ91D magnesium alloy. Studies demonstrate that, besides fabrication defects within the final structure, the element composition plays an important role in the corrosion behavior [37]. The use of aluminum-zinc alloys, as well as rare-earth alloys composed of yttrium, neodymium, cerium, and dysprosium have been explored showing good corrosion behavior and biocompatibility, even though elements such as pure Aluminum are not suitable for biomedical applications [39]. AZ91D was selected for this project since it is a low-cost readily available alloy.

### 3.2 MAGNESIUM WELDING

Being the lightest meta available, magnesium could eventually replace carbon steel and aluminum in structural applications. So far, many aerospace, aircraft, and automotive industry have adopted magnesium for many important applications. As the popularity of magnesium as base material for structural components, the necessity of adequate welding techniques increases. Currently Tungsten-arc inert gas and metal-arc inert gas methods are the preferred at the moment of joining or repairing magnesium-based components[40]. Due to its physical and mechanical properties, many limitations arise when welding magnesium. One of the most challenging obstacles is the rather narrow melting range of this element. The comparative low melting of fusion (645-650°C) requires care from the operator to avoid excessive melting and possible collapse of the welded material[41]. Besides, problems such as oxidation, high coefficient of thermal expansion, and high thermal conductivity, among others must be considered at the moment of joining magnesium components. New welding techniques such as laser and friction-stirring welding in order to overcome these limitations. Nonetheless, drawbacks such as high porosity have been found[40], [42].



Figure 3.1: The use of Tungsten-arc Inert Gas welding for magnesium welding[43].

## Chapter 4: Preliminary work

### 4.1 CREATION OF THE SYSTEM

The first step in the creation of the WAAM equipment was the development of a motion control system. For this purpose, aluminum frames were used in order to allow the fabrication of relatively large and heavy components without compromising the structural integrity of the equipment. The system is capable to move in three axes (X, Y, and Z). Two different frames were created. The first one is used to control the movement of the printing platform in the X and Y axes. This frame is placed horizontally directly over the horizontal plane. The printing bed is belt-driven by two 5V stepper motors (one for each axis). In order to ensure a smooth movement, each axis slides with the use of four barrel-bearings over two steel rods (two bearings per rod). In order to hold the substrate in place, a clamping system made out of aluminum was created (Figure 4.1). Z axis is controlled by an individual frame. A pedestal holding both the torch (heat source) and the wire feeder is screw-driven by a 5V stepper motor. In the first design, another 5V stepper motor was the responsible of feeding the wire; however, no wire diameters larger than 1mm can be efficiently supply by this motor. Thus, a 12V motor (used on a Lincoln Electric 140c MIG welder) is used to feed wire of diameters larger than 1mm. In order to allow an easy change in feeding system, the 5V motor was moved to the superior section of the Z axis frame, this modification can be seen on Figure 4.2. The system is controlled by a couple formed by an Arduino Mega 2650 board and a Ramps 1.4 board. A modified version of the open source firmware Marlin is used as operating environment. Illustration 4.1 shows a schematic of the electronic components required for the proper functioning of the control couple. Controlling couple is shown in Figure 4.3.

Modifications can be done to the WAAM created depending on the desired printing conditions. Two alterations have used in order to study the effects of temperature on the quality of the printed elements. First, water cooled heat extractor was attached underneath the printing bed for the drawing of heat introduced by the heat source. On the other hand, a heating element

(gotten from a Fisher Scientific Magnetic Heated Stirrer) capable to reach up to 800°C was also placed beneath the bed in order to reduce the thermal differential between the areas in which the welding system is passing through and the rest of the printing plate. The original thermostat of the heated stirrer was kept as power supply for the element. Pictures both alterations are shown in Figure 4.4 and Figure 4.5.

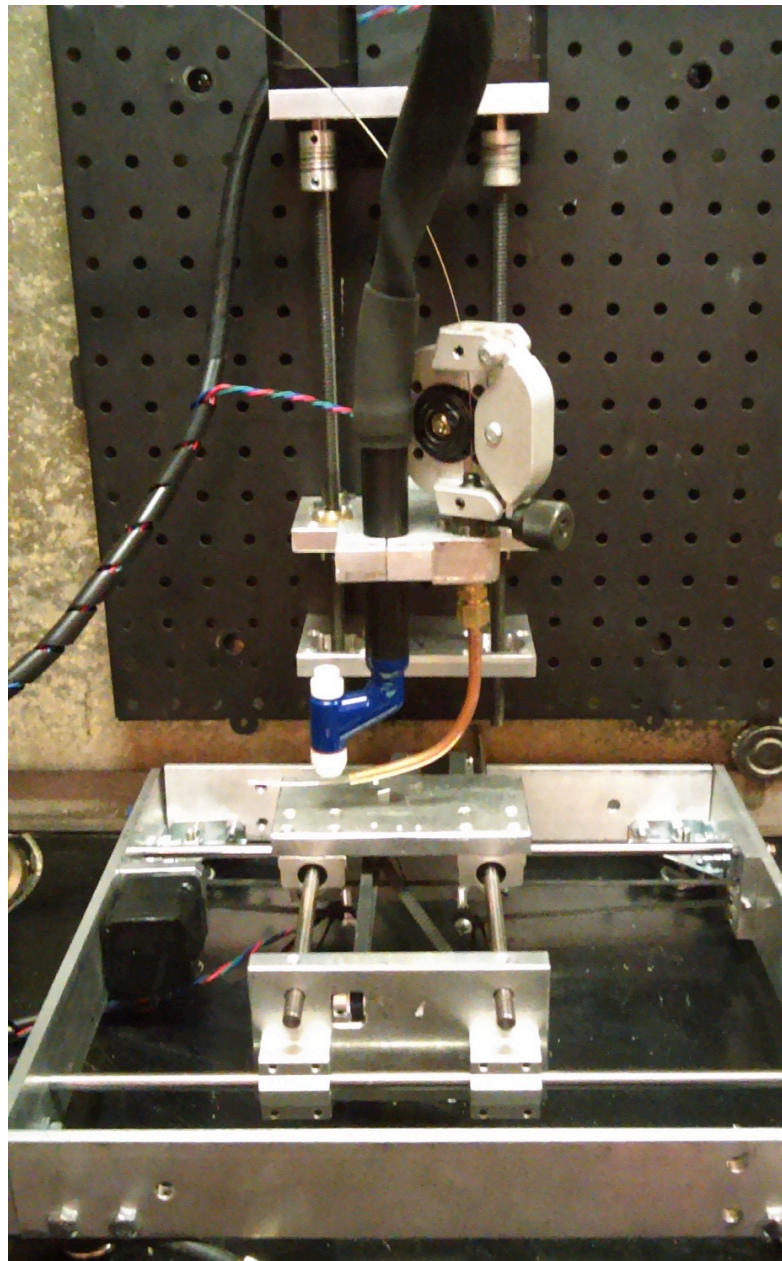


Figure 4.1: First version of the motion system created. X-Y axes controlled by aluminum frame lying on a flat surface. Z axis movement system fixed to the wall. Heat source (plasma torch) and wire feeder (5V stepper motor) fixed on the pedestal.



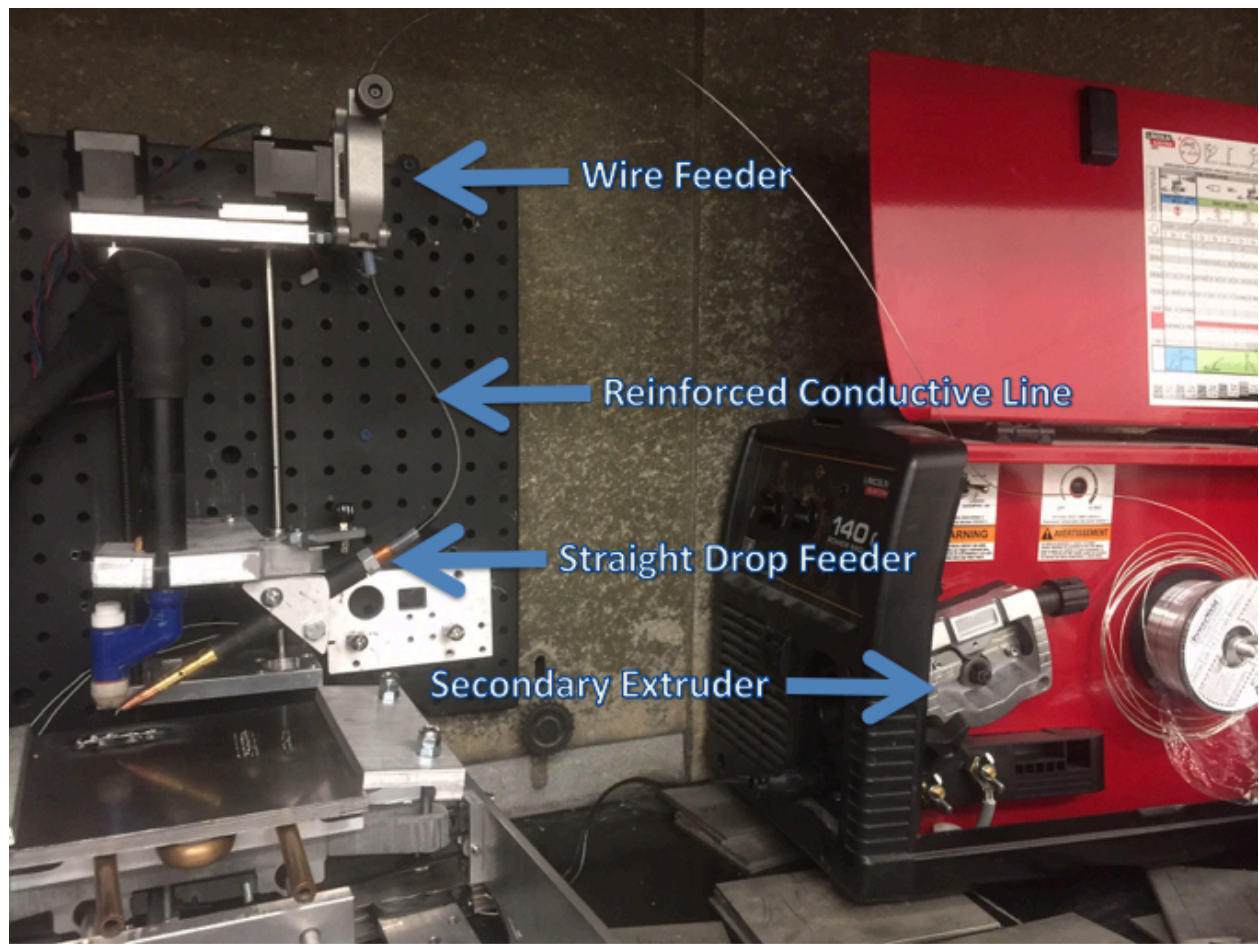


Figure 4.2: Modifications required for the use of filler wire od OD>1mm. “Wire Feeder” being the original 5V stepper motor, while “Secondary Extruder” refers to the 12V motor.

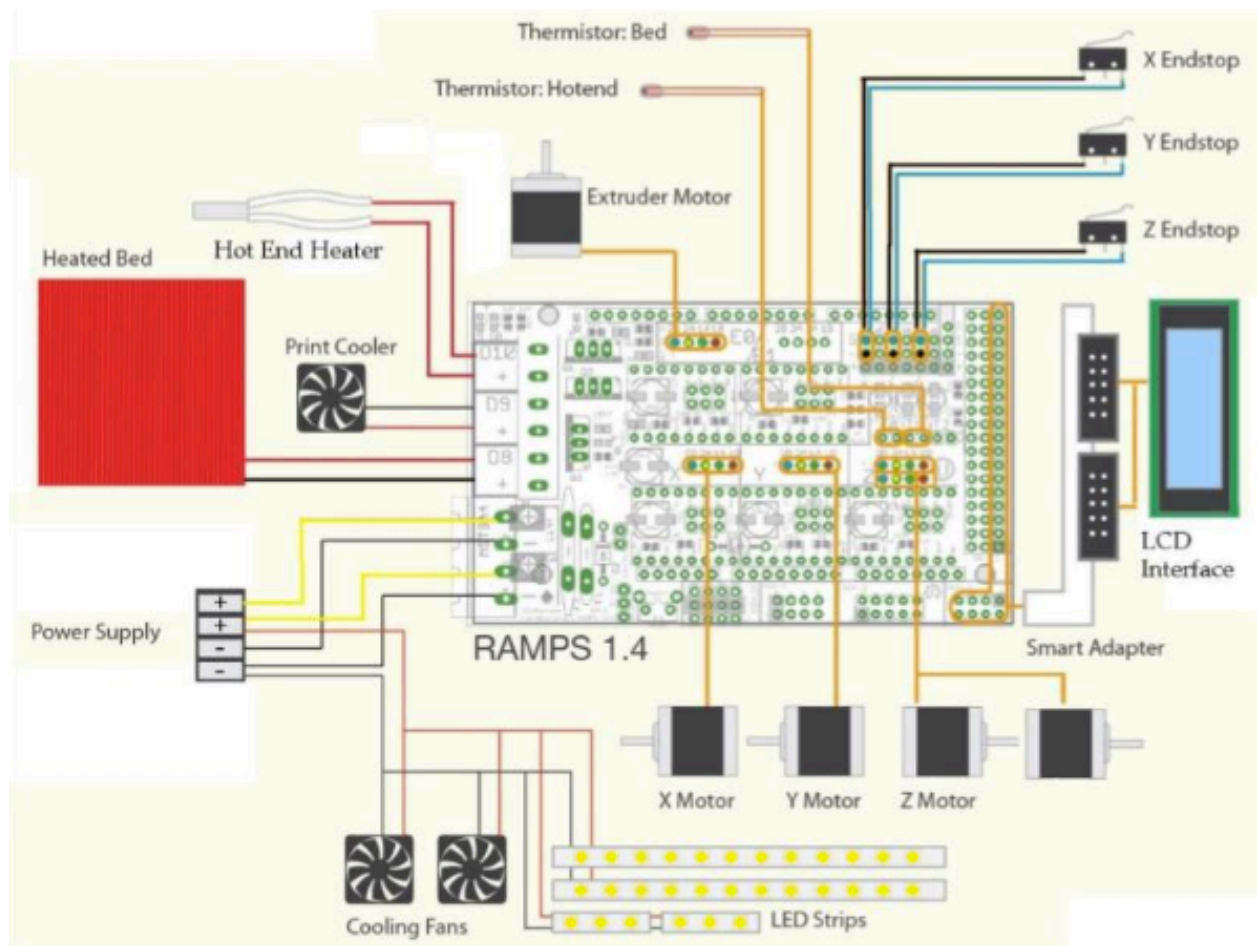


Illustration 4.1: Connection diagram of the components used on the controlling couple [44].



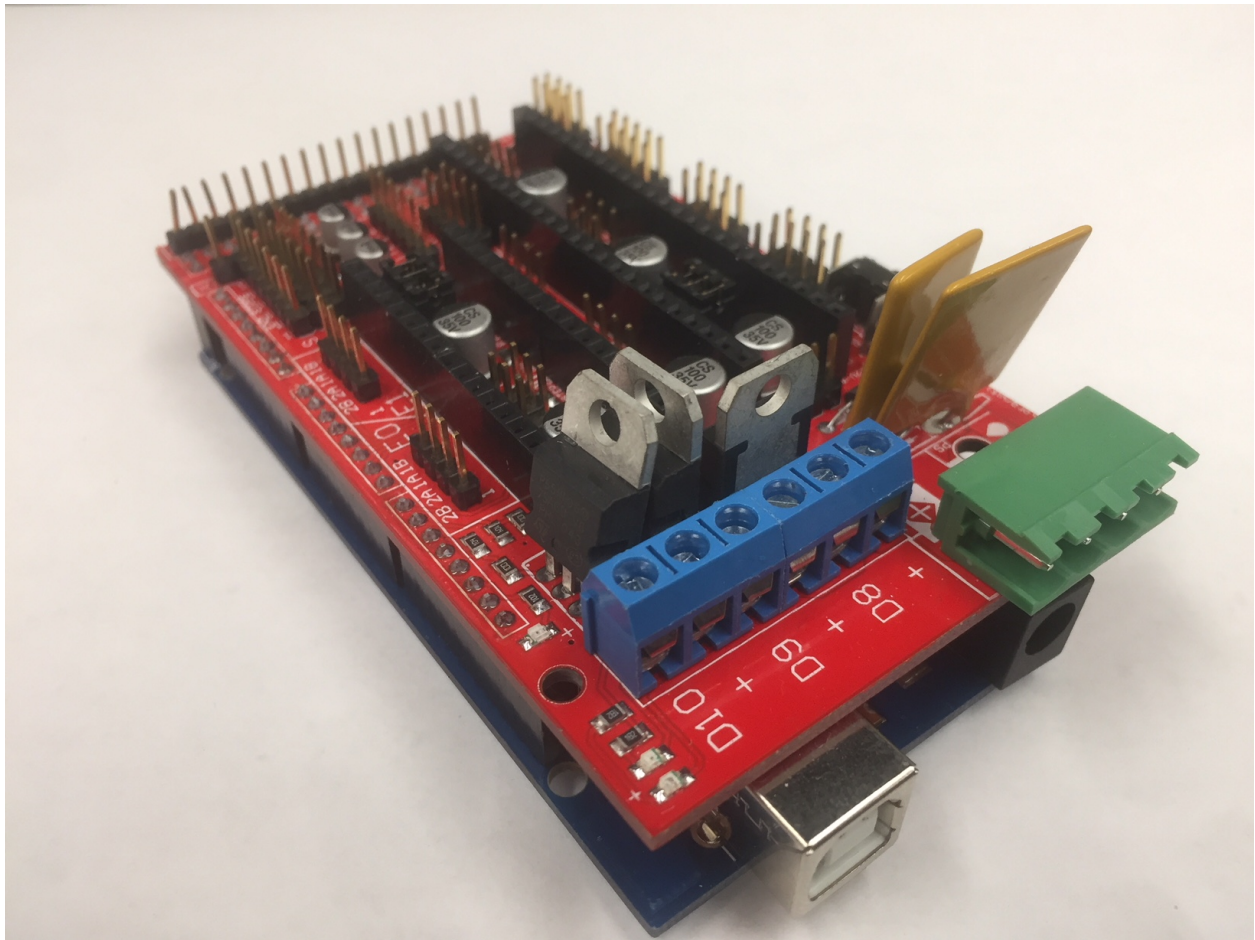


Figure 4.3: Couple formed by the CPU (Arduino Mega 2650, blue board on bottom) and “shield” board (RAMPS 1.4).

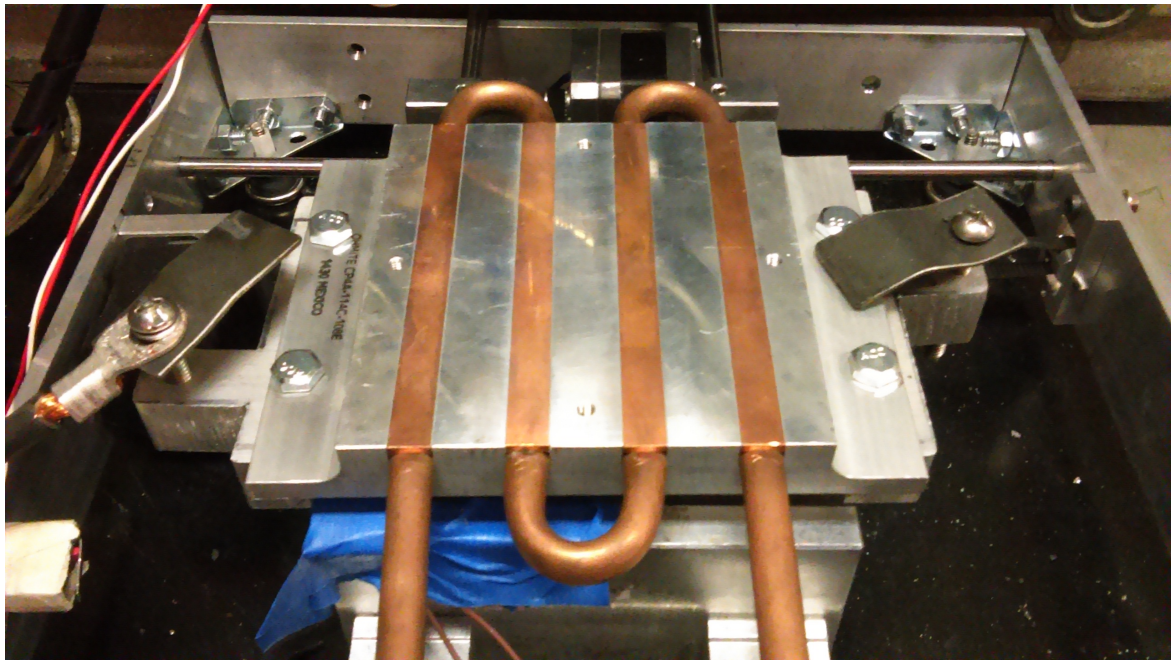


Figure 4.4: X-Y motion control with water cooling system.

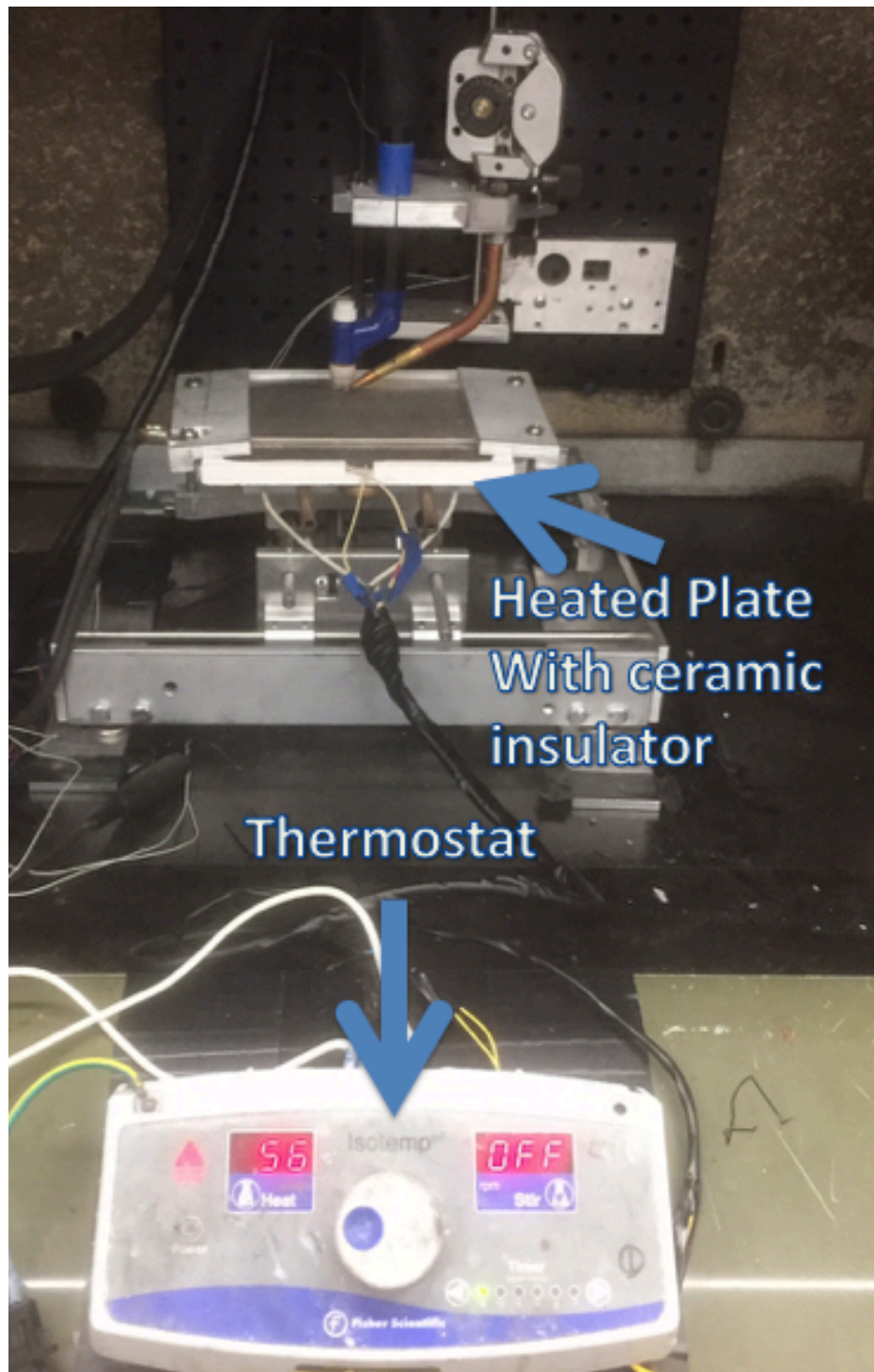


Figure 4.5: Incorporation of a heating element to reduce the temperature differential. The element was placed on top of a ceramic plate to avoid heat induced damage to the moving system.



## 4.2 SELECTION OF POWER SUPPLY AND HEAT SOURCE

A Pro-Fusion Dual Arc 82HFP welding machine was selected since it allows the precise control of the current intensity supplied to the system (Figure 4.6). In low current mode (from 0.1 to 20 Ampere) the parameter can be change by increases of 0.1 Ampere. When working with higher currents (up to 80 Ampere) the steps become of 0.5 Ampere. The incorporation of “Pulsation Mode”, in which the current is supplied in alternating on-off intervals, has been found convenient for the reduction of heat affected zones at the moment of working with stainless steel. The machine is also equipped with a “High Frequency” option, in which the machine sends high frequency pulses through the electrode until a grounded conductive surface is detected. Once a suitable surface is found, an electric arc is automatically started, and the electrode stops emitting high frequency pulses. This mode is highly convenient at the moment of printing, since the arc will not always remain on. Two different heat sources have been used in this project;



Figure 4.6: Pro-Fusion Dual Arc 82HFP welding machine used a power supply.

### **4.3 GAS-TUNGSTEN ARC WELDING (GTAW)**

GTAW, also known as Tungsten-Inert Gas (TIG) is a process in which two metals are molten and joined by the application of heat created by an electric arc established between a non-consumable tungsten electrode and a grounded metallic surface. The element holding the electrode (torch) is connected to a power source as well as to a shielding gas cylinder, as shown in Illustration 4.2. Depending on the desired application, the torch can also be connected to a water cooling system in order to avoid damaged to the internal components that can be produced by the heat when the continue service time is prolonged. The workpiece has to be connected to the other terminal of the power source through a different cable in order to complete to close the electric circuit. In order to protect the weld pool from the air, a shielding gas if directed by a nozzle towards the interest area. When welding thicker sections, a filler material can be fed into the arc. Different polarities can be used in this welding method depending on the desired arc penetration[45].

#### **4.3.1 Direct-Current Electrode Negative (DCEN)**

Also kwon as straight polarity. In this connection configuration, the negative terminal of the power supply is connected to the electrode. The electrode will then emit electrons, which will be accelerated by traveling through the arc, as shown on Illustration 4.3(a). When the electrons enter the workpiece, an amount of energy equivalent to that required for them to be emitted from the electrode is released. In this configuration, about two-thirds of the power is present at the work end of the arc while only one-third remain at the electrode. Thus, a deeper penetration is achieved[46].

#### **4.3.2 Direct Current Electrode Positive (DCEP)**

Also known as reverse polarity. On contrary to DCEN, the positive terminal of the power source is now connected to the electrode. Now, the bigger portion (two-thirds) of energy will remain on the electrode end, while the lower portion will be released to the workpiece. As a

consequence, the resulting weld will be shallow. Since more energy is retained by the electrode, larger electrode diameter and water cooling systems are required in order to prevent tip melting. Illustration 4.3(b) shows the electron flux in this configuration. Intermediate results can be found when Alternate Current is used, as shown in Illustration 4.3(c)[46].

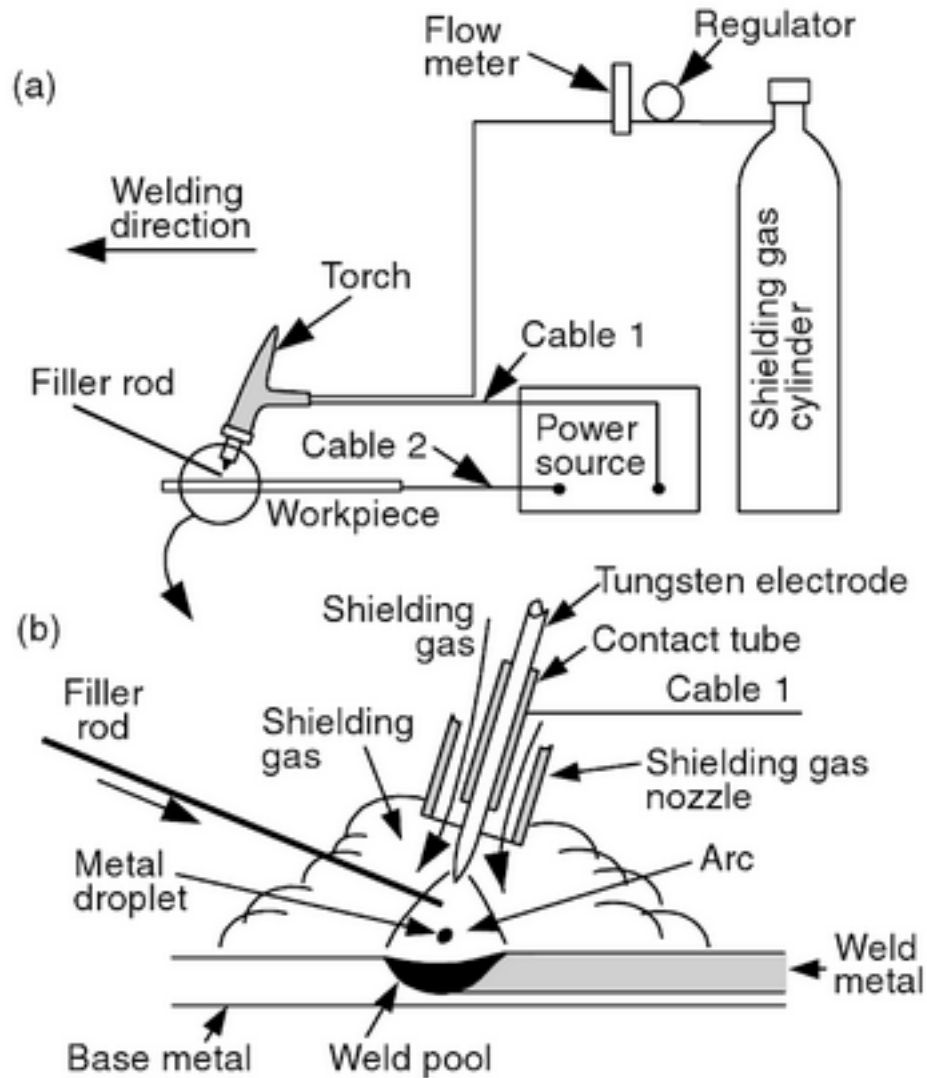


Illustration 4.2: (a) Schematic of the wiring required for GTAW welding. (b) Schematic of the internal components and functioning of GTAW (TIG) torches [46].

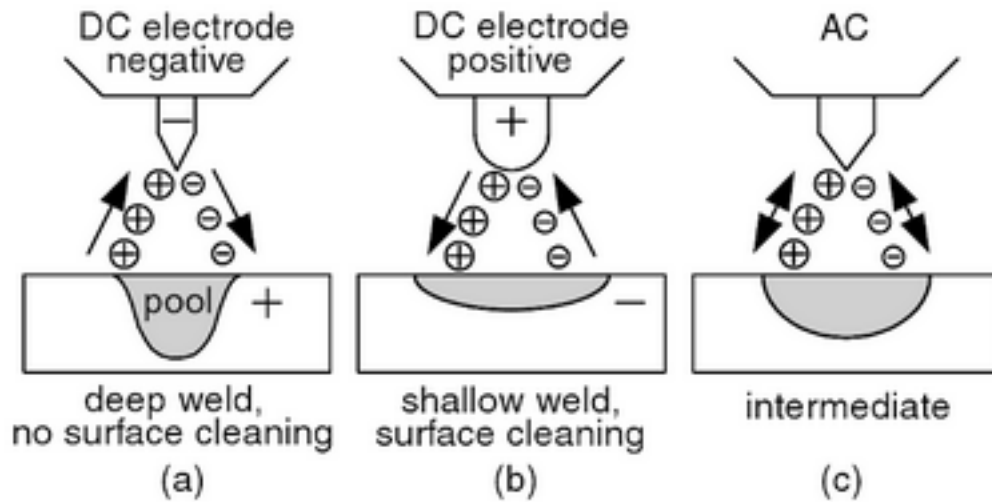


Illustration 4.3: Flow of the current and penetration of the arc as a function of the polarity [46].

Due to its simplicity, cost, and availability, it was believed that this type of torch was the optimum for the project. Problems regarding its intrinsic functioning forced the seeking of a new technique. Two different methods can be used in order to start an electric arc using TIG torches. The most common method, referred as “lift up”, requires the physical contact between the grounded piece of metal over which the arc will be created and the tip of the tungsten electrode. This scheme is highly recommended when welding by hand, since the operator has complete control over the force, angle, and duration of the contact between both elements. Evidently, the created system does not have the required level of sensitivity in order to start the electric arc through this method. As mention previously, high frequency pulses emitted by the power source can also be used to form an electric arc. As a more relievable model, it was decided to use high frequency as the arc starter. Unfortunately, these HF pulses damaged the controlling board immediately, making impossible their use. Many isolation methods were tested, finding no positive results. In order to solve this limitation, the use of Plasma Arc Welding (PAW) was explored.

#### **4.4 PLASMA ARC WELDING (PAW)**

PAW is a process in which two metals are molten and joined by the application of heat created by a constricted electric arc established between a tungsten electrode and a grounded metal. Illustration 4.4(b) shows the internal components of a PAW torch. It can be seen that the electrode does not stick out of the orifice gas nozzle. As shown in Figure 4.7 the arc is collimated as a consequence of the orifice of the gas nozzle. Thus, an arc cannot be initiated by the “Lift Up” method. HF pulses allow a pilot arc to be initiated between the electrode and the orifice gas nozzle. The arc is then created between the electrode and the workpiece by increasing the work current[47].

The use of PAW torch would increase considerably the cost of the project since an additional water cooling system is required for the use of this equipment. However, due to its remarkable advantages over TIG torches, a PLT-100M0 plasma torch and a Pro-Fusion Water Cooling System were bought. The internal array of a plasma torch does not allow for the HF pulses to get out of the torch’s nozzle, solving the problematic behind the change in welding technique. Besides, PAW systems are known to create a more focalized, linear arc, in contrast to TIG torches that create a wider, bell-shaped arc. Also, the stability of the plasma arc is superior to that created by TIG.



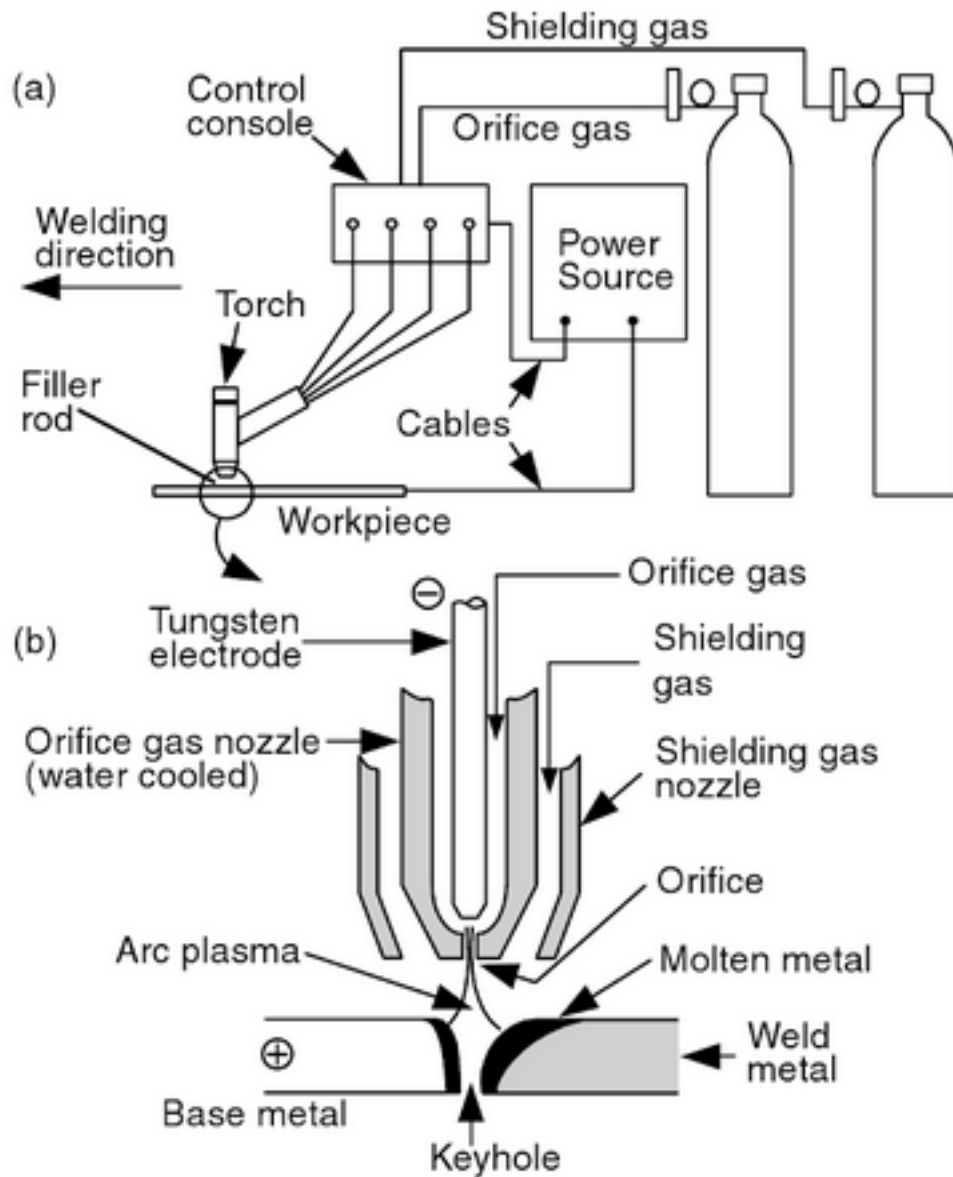


Illustration 4.4: (a) Wiring diagram of Plasma Arc Welding. (b) Internal components of PAW torch [46].

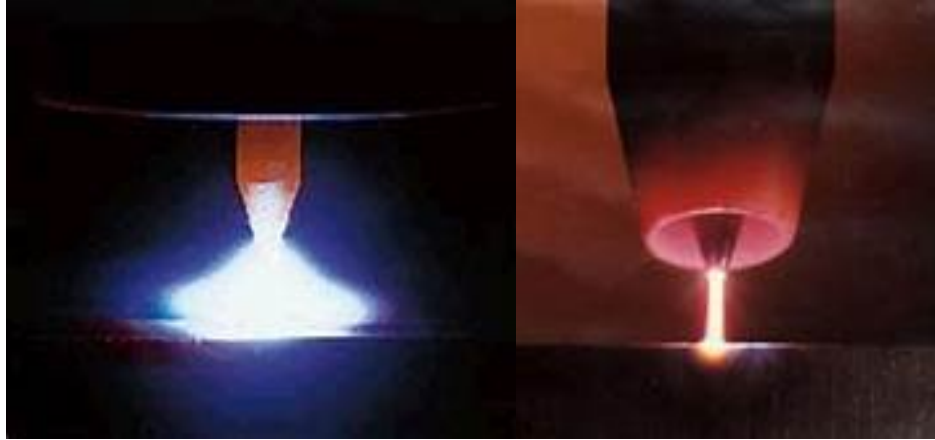


Figure 4.7: Comparison between Gas-Tungsten arc (Left) and Plasma arc (right) [48].

#### 4.5 SYSTEM FUNCTIONING

The created WAAM systems rely on the use of a plasma arc for the melting and fusing of a metallic wire (filler) and a printing bed (substrate). The wire is being fed by either a 5V stepper motor or a 12V motor through a reinforced conduction line and delivered to the molten metal pool created by the arc. As the printing bed moves, the fusion between the wire and the substrate forms a 3D line, which dimensions and morphology would depend on different factors. Printing bed speed, wire diameter, arc current intensity, the wire delivering position, and wire feeding speed, are variables which changes will impact directly the final product. Adjacent lines can be created by directly overlapping the line already printed and the printing path of the new line. The relative position of the arc and the wire must be kept in all time in order to obtain good results, as Illustration 4.5(II) displays. Also, lines can be printed upon previous weld lines in order to create 3D structures.

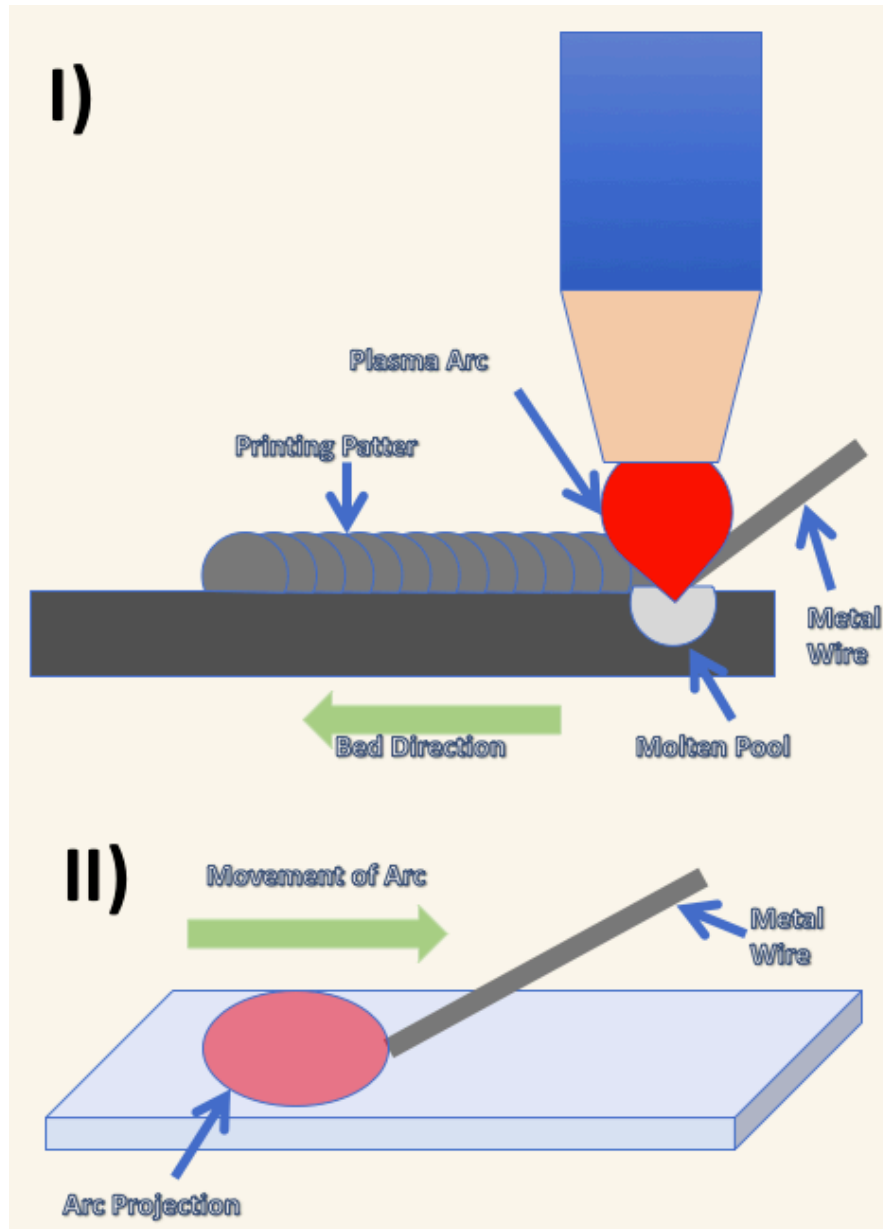


Illustration 4.5: I) Diagram of the functioning of the WAAM system created. II) Relative position of the arc and wire required for good results.

## **Chapter 5: Experimental Procedure**

### **5.1 MATERIALS**

The use of Aluminum-Zinc alloys, as well as rare-earth alloys composed of yttrium, neodymium, cerium, and dysprosium have been explored showing good corrosion behavior and biocompatibility, even though elements such as pure aluminum are not suitable for biomedical applications [39]. AZ91D was selected since it is a low cost, readily available alloy when compared to products alloyed with rare earths. The product used for this project was manufactured by China Hunan High Broad New Material Co. Ltd. In order to get better resolution in the final printed structures, small wire diameter is required. Due to its brittle properties, the smaller commercial AZ91D wire diameter that could be obtained was 1.5mm., being this size the selected for the research. As substrate, 3mm (1/8") Stainless Steel 316 plate was used. This material was gotten from Aarmor Metal & Supply Inc. The contrast in properties between the filler and substrate materials allows the temporary adhesion, thus, after printing, the magnesium specimens can be easily detached from the substrate.

#### **5.1.1 Magnesium alloy AZ91D.**

This magnesium-aluminum-zinc alloy is the most widely used metal for die casting, hence the letter D at the end of the nomenclature. Even though its machinability is limited, this process can be performed having special precautions[49]. Table 5.1 shows the typical chemical composition. Tables 5.2 and 5.3 respectively display the physical and mechanical properties of this specific alloy. The corrosion rate of the alloy is low as a consequence of the reduced levels of impurities such as iron, copper, and nickel (Table 5.1). The corrosion behavior of AZ91D in the presence of living cells has been studied. It was proven that live cells can be cultivated on this alloy. However, the adhesion and spreading of the organisms is limited due to the change in pH caused by the corrosion products generated by the alloy. Moreover, the corrosion of samples with adhered cells is lower to those in which no cells were cultivated since they act as a physical barrier and the corrosive reaction is then slowed down [50]. It has also been proved that the use

of protective coatings, such as CrO and nickel, decrease the corrosion rate in vivo of AZ91D specimens [51].

Table 5.1: Chemical composition of magnesium alloy AZ91D[52].

<i>Alloy</i>	<i>Al</i>	<i>Zn</i>	<i>Si</i>	<i>Mn</i>	<i>Cu</i>	<i>Fe</i>	<i>Ni</i>	<i>Others</i>	<i>Mg</i>
<i>AZ91D</i>	8.5-9.5	0.45-0.90	0.05max	0.17min	0.015max	0.004max	0.001max	0.01max	balance

Table 5.2 Physical properties of magnesium alloy AZ91D[52].

<i>Property</i>	<i>AZ91D</i>
<i>Specific gravity (g/cm<sup>3</sup>)</i>	1.81
<i>Solidification range ( °C)</i>	596-568
<i>Specific heat (J/kg K)</i>	0.98
<i>Thermal Conductivity (W/m K)</i>	52
<i>Thermal expansion coefficient (10<sup>-6</sup>/K)</i>	26
<i>Heat of fusion (kJ/kg)</i>	372.4

Table 5.3: Mechanical properties of magnesium alloy AZ91D[52].

<i>Property</i>	<i>AZ91D</i>
<i>Tensile strength (MPa)</i>	196-255
<i>0.2% proof stress (MPa)</i>	147-167
<i>Elongation (%)</i>	0.5-3
<i>Brinell hardness</i>	65-68
<i>Young's modulus (GPa)</i>	44
<i>Fatigue strength (MPa-5x10<sup>7</sup> cycles)</i>	49-69

### 5.1.2 Stainless Steel 316

Iron-based alloys containing a minimum amount of 10.5wt% of chromium are denominated Stainless Steel. In contact with oxygen, these materials form a self-healing and adhesive passive layer ( $\text{CrO}$ ) which protects the alloy from corrosion[53]. In contrast with galvanized steels, which are coated with zinc or cadmium in order to form a galvanic couple, stainless steels keep their corrosion resistance no matter how much material is removed from the surface. Besides chromium, elements such as molybdenum and nickel are added to enhance the mechanical and corrosion resistance properties of these alloys. The nomenclature used for the categorization of stainless steels is unusual, since it is based on the nature of their metallurgical structure[54]. Thus, depending on the chemical compositions, the microstructure may be composed by austenite or ferrite, a mixture of these two (duplex), martensite, or a precipitation hardened structure. Figure 5.1 shows the changes in microstructure as a function of the amount of nickel and chromium added to the alloy[54].

Stainless Steel 316 is the second most widely used austenitic stainless still (on behind SS 304). It incorporates molybdenum in its composition, which gives the system enhanced corrosion resistance properties. Due to its high formability and weldability, it has been incorporated in many applications in the industry, architecture, transportation, among many other sectors. Table 5.4 shows the chemical composition and Tables 5.5 and 5.6 the physical and mechanical properties of this alloy respectively. SS316 exhibit good oxidation resistance at elevated service temperatures. Their properties are retained in intermittent service at  $870^{\circ}\text{C}$  and under continues service at  $925^{\circ}\text{C}$ [54].

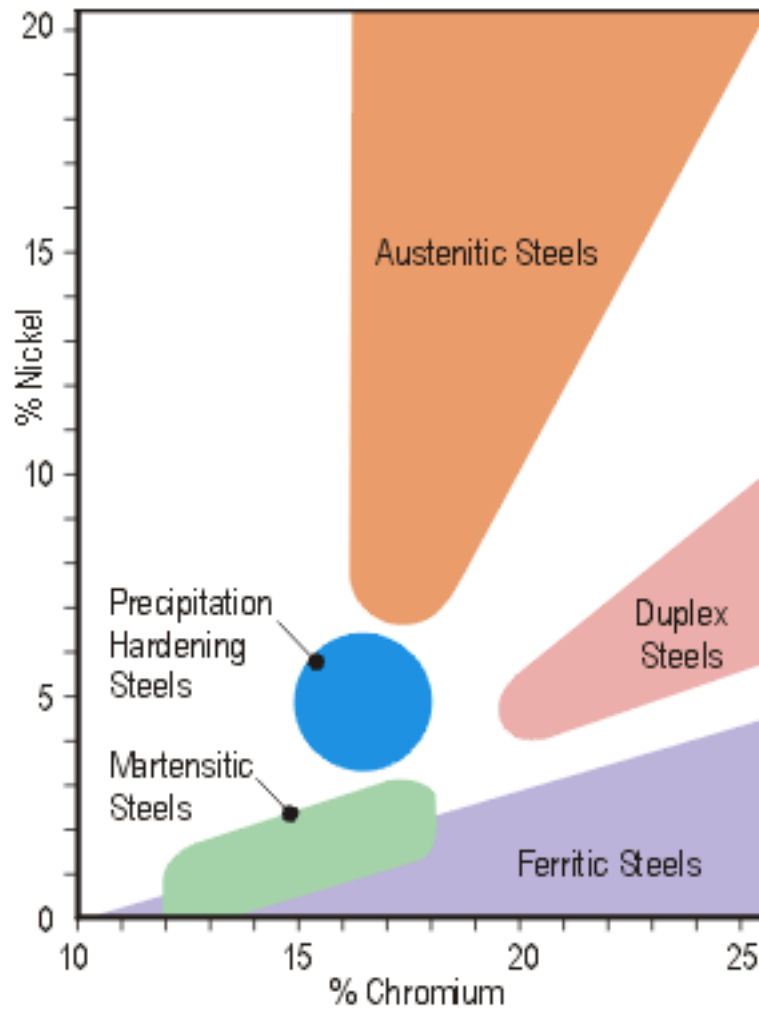


Figure 5.1: Change in microstructure as a function of the alloying content[54].

Table 5.4: Chemical composition of Stainless Steel 316[54].

<i>Alloy</i>	<i>C</i>	<i>Cr</i>	<i>Ni</i>	<i>Mo</i>	<i>Mn</i>	<i>Si</i>	<i>P</i>	<i>S</i>	<i>Fe</i>
<i>SS316</i>	0.03max	16-18.5	10-14	2-3	2max	1max	0.045max	0.03max	balance

Table 5.5 Physical properties of Stainless Steel 316[54].

<i>Property</i>	<i>SS316</i>
<i>Specific gravity (g/cm<sup>3</sup>)</i>	8
<i>Specific heat (J/kg K)</i>	500
<i>Thermal Conductivity (W/m K)</i>	21.5
<i>Thermal expansion coefficient (10<sup>-6</sup>/K)</i>	16.2
<i>Electrical Resistivity (nΩ.m)</i>	740

Table 5.6: Mechanical properties of Stainless Steel 316[54].

<i>Property</i>	<i>SS316</i>
<i>Tensile strength (MPa)</i>	515
<i>0.2% proof stress (MPa)</i>	205
<i>Elongation (%)</i>	40
<i>Brinell hardness</i>	217
<i>Young's modulus (GPa)</i>	193

The contrast in properties between the filler (magnesium alloy AZ91D) and substrate SS316) allows the temporary adhesion, thus, after printing, the magnesium specimens can be easily detached from the substrate. Moreover, the resistance to oxidation at high temperatures that SS316, as well as its weldability, make it a great option for its use as printing bed.

The main objectives of the performed experiment were; 1) Determine the optimal parameters in which visually uniform metal base line could be printed; and 2) Analyze and characterize the resulting lines in order to determine the internal integrity of the lines as a function of the different printing parameters.



## 5.2 DETERMINATION OF OPTIMAL PRINTING PARAMETERS

In order to find which combinations of parameters yield the best results a series of trials using different printing parameters were performed. Parameters related with the intensity of the arc were first found by a trial-and-error method. It was found that one of the main factors that affect the quality of the line was the gas flow rate of the pilot arc. When the flow rate is low ( $<0.4$  L/min) the arc was not able to melt the wire. On the other hand, high flow rates ( $>0.8$  L/min) create a strong jet that carve the substrate and ejects the molten metal wire away from the molten pool. Thus, a medium pilot arc gas flow rate was used (0.6 L/min). In order to protect the molten pool from the air, a shielding gas flow rate of 12 L/min was used for all the trials. For both the pilot gas and the shielding gas 99.99% Argon was used.

Due to technical limitations, the wire feed rate had to be kept constant. Since the cross-section area of the selected filler was superior to 1mm (wire diameter=1.5mm) the 12V motor was used. The minimum feed rate that the motor is capable to produce is 117cm/min (46in/min). This feed rate was then used for all the trials. The delivery angle of the wire, as well as the position were also kept fixed for all the explored conditions. Figure 4.5(II) shows the delivery position of the filler.

Once determined the parameters that would remain fixed, a series of trails in which only the printing speed and the arc current intensity changed were performed. As the substrate speed changes, the amount of heat supplied to the substrate was also altered. Lower speeds would allow the torch to introduce more heat to the bed, since the arc was over it for a longer period of time. Also, as the current supplied by the power source increases, the amount of heat generated by the plasma arc also increases. Thus, the combination of parameters that would introduce more heat to the substrate are those in which the printing speeds are low, and the current is high.

Figure 5.2 shows a visual representation of the combination of parameters that were used on the trials to determine the best printing conditions. Printing speed was changed from 90 to 180 mm/min, using intervals of 15 mm/min between each trial. 20 to 50 Ampere were tried. This time, the intervals were kept on 5A between each trial. A window of parameters in which

visually uniform lines could be printed was found. 15 parameters inside this printing window were selected (5 current intensities; 30A, 32.5A, 35A, 37.5A, and 40A, and 3 printing speeds 120mm/min, 135mm/min, 150mm/min). Using each one of these combinations, 5 parallel lines were printed over the same substrate. After printing, the lines were detached from the substrate and their dimensions were measured. Then they were sectioned and mounted in epoxy resin for further analysis and characterization. In order to produce the least amount of damage, an abrasive cut-off saw was used, following recommendations for metallography of magnesium and its alloys[55].

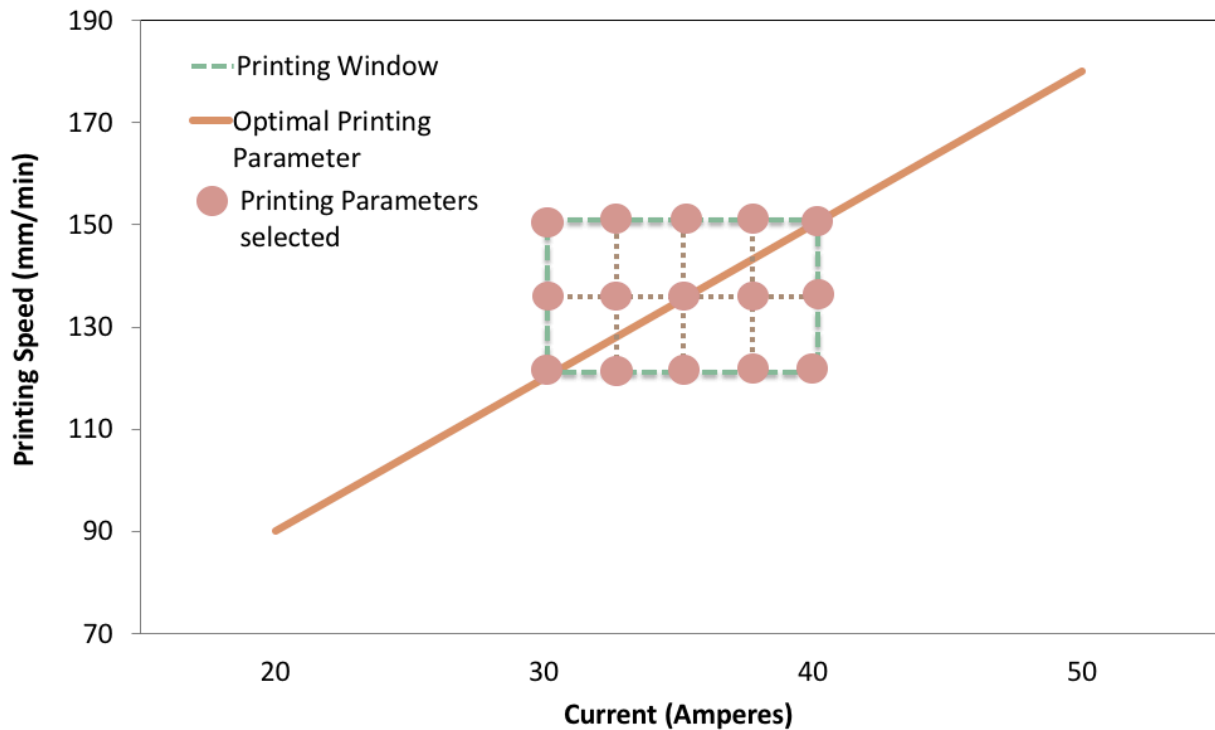


Figure 5.2: Visual representation of the selection of printing parameters.

### **5.3 ANALYSIS AND CHARACTERIZATION**

After printing, the lines were measure in order to determine any possible relationship between the printing parameters and the resulting lines. After sectioned and mounted, polishing and etching was performed. The samples were wet grinded using a series of graded abrasive papers (240,400,600,800,1200, and P4000), changing the grinding direction between each other grid. Glycol (1ml HNO<sub>3</sub>, 24mL water, 75mL Ethylene Glycol) was used as etchant, since it is recommended for general purpose etching[55]. The specimens were submerged in the etchant agent for 10 seconds, rinsed with distilled water, and dried with air. After polishing and etching, the specimens were analyzed by the following techniques;

#### **5.3.1 Optical Microscopy**

The name of this technique arises from the use of visible light for the detection of features present in the surface of the specimen. Optical microscopy is, to date, the most popular and most widely used tool for research purposes. In this characterization technique, a specimen (called objective) is placed between one and two focal lengths from an objective lens[56]. Reflected light rays created by the object are first converged with the use of a lens (objective lens). Then, they are focused to form a magnified, but inverted, image. Finally, these magnified light rays are converged by a second lens, called projector lens, to form the final image. The light rays generated by the projector lens will create a real image only when seen on a screen or a camera film. If the examination has to be conducted with the eyes, the use of an eyepiece is required. The virtual image created by projector lens is inverted by the eyepiece to have accurate sight of the real image[56].

The optical microscope used for this project was a KEYENCE VHX-900 Digital Microscope equipped with a VH-Z100UR lens (Figure 5.3). Micrographs at magnifications of 100X were captured from 6 different sections of the cross-section area of the printed lines (Bottom right corner, bottom left corner, upper right shoulder, upper left shoulder, top, and center of the specimens). 1000X micrographs were also taken from the central area of all

samples in order to find microstructural changes between lines printed using different parameters. Longitudinal sections of printed lines were also analyzed at 100X and 1000X. In this case, the location from which the micrographs were gotten is irrelevant.

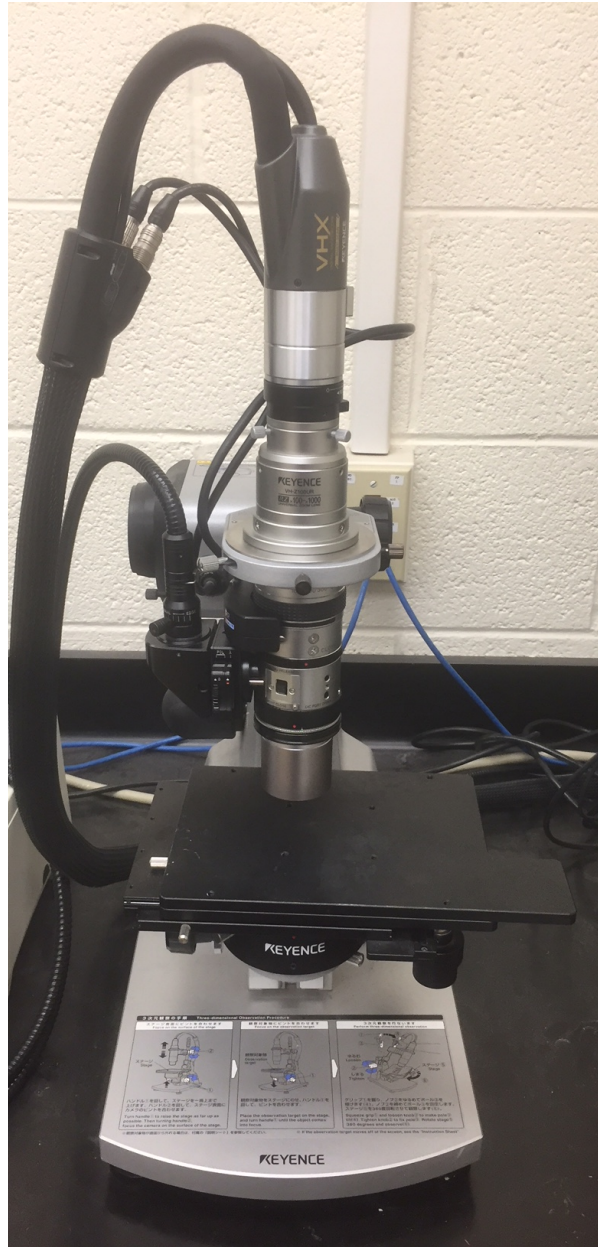


Figure 5.3: KEYENCE VHX-900 Digital Microscope equipped with a VH-Z100UR lens used for optical microscopy.

### 5.3.2 X-Ray Diffractometry

The use of X-rays allows the identification of materials by their crystal structure, not by the elements present on them or their composition. Thus, materials having the same composition can be individually identified. For this reason, characterization techniques that rely on X-rays are the most trust-worthy methods for the determination of both crystal structure and chemical composition of materials. X-rays are high-energy and short-wavelength beams of electromagnetic radiation generated by the collision of accelerated electrons against a metal target [56]. As a consequence of the impact, a rapid deceleration of the electrons makes possible the transformation of the kinetic energy into X-ray radiation. A diffractometer is designed to detect and record the diffraction intensity of x-rays as a function of the diffraction angle ( $2\theta$ ) created by a material. The radiation generated by the X-ray tube is collimated by slits in order to prevent beam divergence. In order to suppress any wavelength other than the desired, a monochromatic filter is used. Continuous change in the incident angle of the X-ray beam generates a spectrum of diffracted intensity against diffraction angle. The recorded spectra is then compared with a database containing over 60,000 different spectra of known crystalline substances [56].

A Bruker XRD D8 system using Cu  $K_\alpha$  ( $\lambda=1.54 \text{ \AA}$ ) X-ray source (Figure 5.4) was used to for the analysis of the as-received wire, printed lines, and two by-products formed during the printing process. A 0.2mm slit was used on the source and a 6mm slit was used on the detector. For all the cases, the reading took place from  $10^\circ$  to  $80^\circ$  with steps of  $0.020^\circ$  and scanning speed of 1 second/step.

### 5.3.3 Scanning Electron Microscopy.

The Scanning Electron Microscopy (SEM) is the most widely used type of electron microscope [56]. In this characterization technique, a focused electron beam that scans over the surface of the analyzed specimen forms the image. Due to its high depth of field, SEM creates images with three-dimensional appearance. In contrast with other electron microscopes, such as transmission electron microscopes, its operation and maintenance are relatively simple.

Moreover, chemical information can be obtained by the equipment of X-ray Energy-Dispersive Spectrometer (EDS). A basic SEM consists of an electron gun and a series of electromagnetic lenses and apertures, which generate a condensed probe that scans the surface of the specimen. Depending on the desired magnification, different electron beam sources can be used. Thermionic sources can generate images up to 10,000X, while field emission sources only reach 10-100X[56]. The use of SEM for this project was only to determine the chemical composition of the printed specimens at different locations within the cross-section area.

For this project, the use of SEM was limited to obtaining reference images for EDS mapping. A Hitachi S4800 equipped with EDS (Figure 5.5) was used. Three different areas of the cross-section area were analyzed (bottom, center, and top). The accelerating voltage was 10kV for all the cases.



Figure 5.4: Bruker XRD D8 system used in this project [57].

### 5.3.4 Electron-Dispersive Spectrometer

This technique relies on the use of characteristic electrons emitted from a solid element. Two different electrons can be used for this purpose, either Auger electrons or photoelectrons. In both cases, characteristic energy levels, that would reveal the nature of the chemical elements present in the specimens, are recorded. A downside of this technique is that both electrons can only be emitted from the uppermost atomic layers of the samples (no more than 10nm). Thus, only surface chemical analysis can be obtained. Using this technique, an elemental mapping of different section on the cross-section area of the specimens.



Figure 5.5: Example of Hitachi S4800 SEM equipped with EDAX EDS system.



## Chapter 6: Results

### 6.1: CHARACTERIZATION OF AS-RECEIVED AZ91D WIRE

With the use of optical microscopy, the as microstructure of the as received AZ91D wire was analyzed. Figure 6.1 shows a micrograph of a longitudinal cut of the feedstock. It can be seen that a fairly equiaxed gran structure, with an average grain size of  $3.35\mu\text{m}$ . The presence of equiaxed grains indicates that the wire was rolled at high temperatures and the cooled by air. The slow heat dissipation inside the wire coil made possible conditions similar to those required for annealing, hence the final microstructure[58]. The presence of second phase particles aligned on the rolling direction can also be seen. The presence of defects was also detected (points A and B). XRD spectra (Figure 6.2) demonstrate the presence of  $Mg_{17}Al_{12}$  ( $\beta$  phase) embedded on a pure magnesium matrix ( $\alpha$  phase).

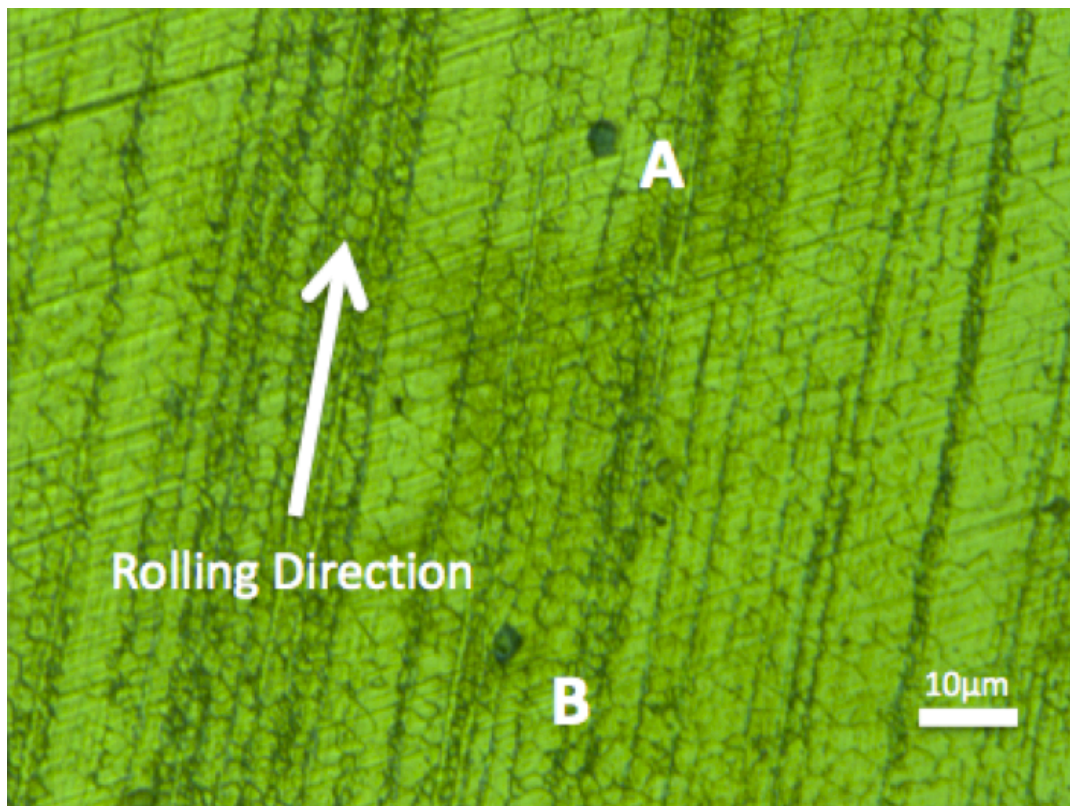


Figure 6.1: Optical micrograph of a longitudinal cut of the as-received AZ91D wire. 1000X. Etched with glycol.



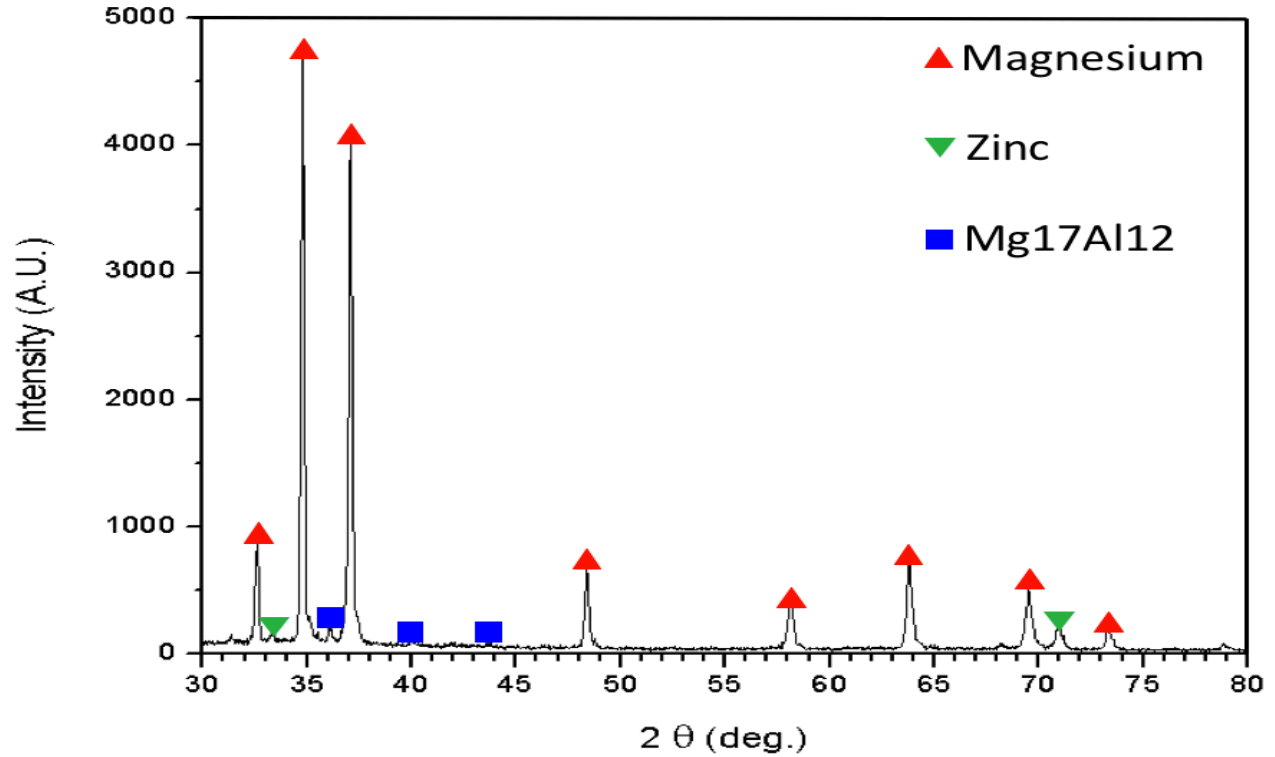


Figure 6.2: XRD spectra of as-received wire. Representative peaks of magnesium ( $\alpha$  phase), zinc, and  $Mg_{17}Al_{12}$  precipitates ( $\beta$  phase).

## 6.2: MACROSCOPICAL FEATURES

Figure 6.3 shows representative lines printed over a range of printing conditions. Low temperature conditions can be achieved by using fast moving speed and applying low arc current, such as the case of condition A. In this case, it is noticeable that the wire did not completely melt. Traces of the original wire can be seen in many points of the line. When dealing with low currents (20A-30A) but low printing speeds, such as the case of condition B, tumulus of fully molten metal can be seen. It is believed that the high amount of materials deposited due to the low speeds made created the partition of the original line. On contrary cases, when high currents (>40A) the metal wire becomes highly fluid. Thus, at printing speeds superior than 170mm/min (condition D), the molten metal will flow and congregate on the beginning of the printed line, since it is the first solidified region. At lower speeds (<160mm/min) the molten metal has more time for its solidification. For this reason, the molten

metal will flow and conglomerate in those places where the liquid metal has become solid, as seen on conditions E.

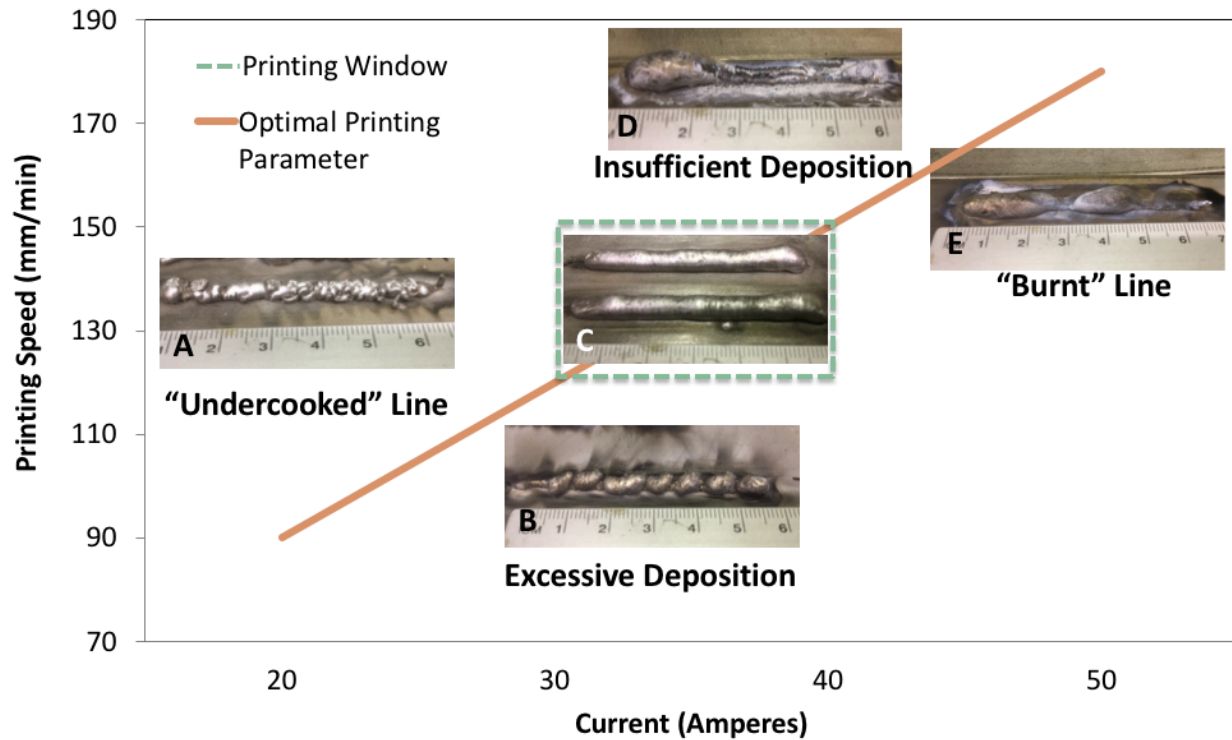


Figure 6.3: Visual representation of the macroscopical appearance of printed lines created under different printing conditions.

Printing conditions in which mostly visually uniform lines can be printed was found. The combination of medium arc currents and relatively low printing speeds yielded the best results. C shows representative lines printed under conditions laying in this "printing window". It can be seen, however, that in a similar manner than those high heat condition (D & E), the material tend to conglomerate on the beginning of each printed line (right hand side). As it is expected, depending on the printing conditions, the temperature on the printing plate will increase as the number of lines printed in the same plate increases. Figure 6.4 shows the increase in printing bed temperature under two printing condition. The lowest printing temperature represent that in

which the arc current was the lowest used (30A) and the printing speed was the highest (150 mm/min). On the other hand, the highest temperature printing condition is that in which the highest arc current (40A) and the lowest printing speed (120 mm/min) were used. After printing the all the specimens, it was noticed that the ability for the lines to be easily detached from the printing plate decreases as the number of lines printed in the same plate increased. Also, when using printing parameters that introduce the highest amounts of heat to the substrate (especially those using an arc current of 40A), some lines were impossible to detach from the plate. Any line printed when the temperature on the printing plate is below 170°C can be easily detached from the substrate as shown in Figure 6.4. Figure 6.5 demonstrate the easy separation of the printing lines when the temperature of the printing bed does not exceed the critical temperature of 170°C. Under many of the printing conditions, the last line printed was impossible to detach using pliers (as shown in Figure 6.5). For the highest heat condition, only 3 lines could be detached. Thus, only 3 lines from each condition were used.

Small fluctuation in the width and height within the same printed line were found. Variation in size also occurs when measuring the average dimensions of the different lines printed under the same conditions in the same plate. As mentioned previously, only 3 out of the 5 lines printed were used. No correlation between any printing condition nor the number of lines printed in the same plate and the dimensions of the line was found. Tables 6.1 and 6.2 show the average height and width respectively for each printed line under all the printing conditions. The standard deviation in the measurements was calculated as a function of the printing speed and the arc current for both dimensions, height and width (Tables 6.3-6.6).

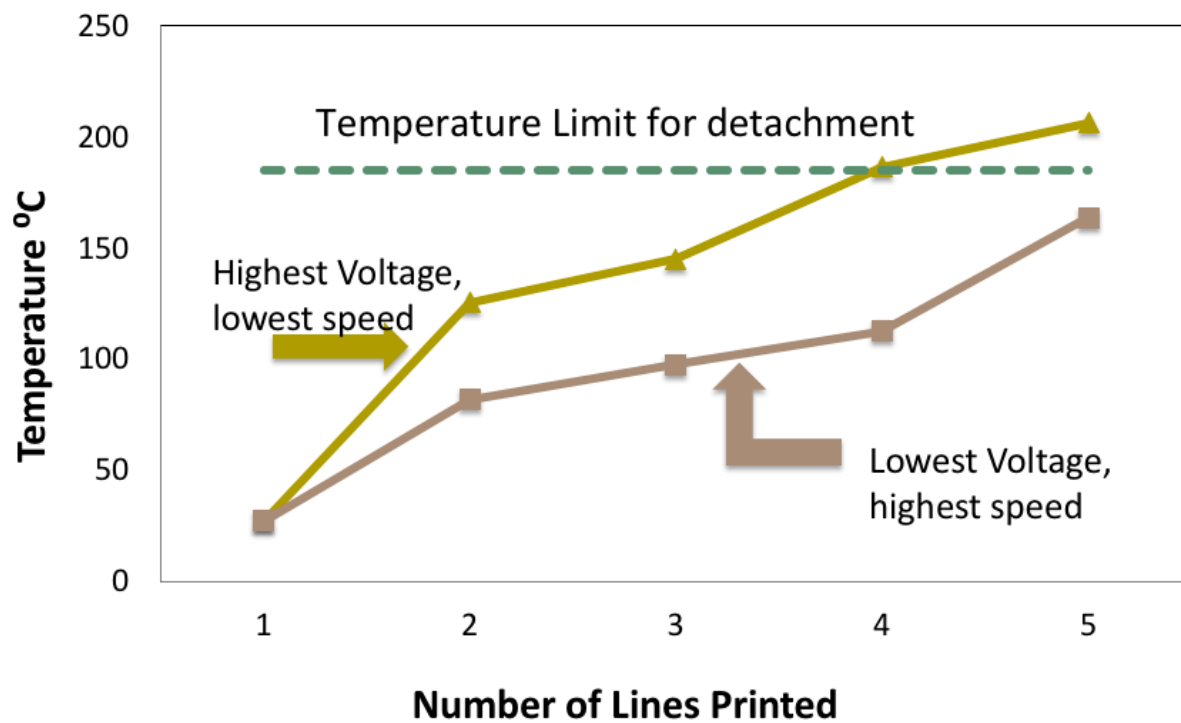


Figure 6.4: Increase in the temperature of the printing plate under two different printing conditions (lowest and highest heat input) as the number of lines printed increases. Critical temperature for detachment shown by dashed lines.



Figure 6.5: Sequence of steps for the detachment of lines from printing plate. I) Firmly hold the line with pliers. II) Twist the printed line to break the temporary bond. III) Separate the line from the substrate.

Table 6.1: Average width and standard deviation of printed lines under all the printing parameters.

Current(Amps)	Speed(mm/min)	W1 (mm)	W2 (mm)	W3 (mm)	$\sigma$ (mm)
<b>30</b>	<b>120</b>	5.72	5.67	5.86	0.10
	<b>135</b>	5.75	5.84	5.74	0.06
	<b>150</b>	5.85	5.34	5.45	0.27
<b>32.5</b>	<b>120</b>	5.64	5.93	6.56	0.47
	<b>135</b>	5.82	5.28	5.31	0.30
	<b>150</b>	6.60	5.91	5.78	0.44
<b>35</b>	<b>120</b>	5.44	6.43	7.23	0.90
	<b>135</b>	5.57	6.28	5.73	0.37
	<b>150</b>	5.28	5.31	5.66	0.22
<b>37.5</b>	<b>120</b>	6.56	5.83	6.16	0.37
	<b>135</b>	5.44	5.53	6.40	0.53
	<b>150</b>	5.78	6.05	6.02	0.15
<b>40</b>	<b>120</b>	7.26	6.72	6.03	0.62
	<b>135</b>	6.46	6.39	6.14	0.17
	<b>150</b>	6.92	6.14	6.09	0.47

Table 6.2: Average height and standard deviation of printed lines under all the printing parameters.

Current(Amps)	Speed(mm/min)	H1 (mm)	H2 (mm)	H3 (mm)	$\sigma$ (mm)
<b>30</b>	<b>120</b>	4.40	4.21	4.33	0.09
	<b>135</b>	4.49	4.28	4.10	0.20
	<b>150</b>	3.88	3.68	3.67	0.12
<b>32.5</b>	<b>120</b>	4.12	3.99	4.19	0.10
	<b>135</b>	3.81	3.82	4.02	0.12
	<b>150</b>	4.09	4.00	3.79	0.15
<b>35</b>	<b>120</b>	3.63	3.75	3.72	0.07
	<b>135</b>	3.60	3.39	3.68	0.15
	<b>150</b>	3.61	3.51	3.67	0.08
<b>37.5</b>	<b>120</b>	4.11	4.15	3.63	0.29
	<b>135</b>	3.72	3.74	3.60	0.08
	<b>150</b>	3.72	3.66	3.48	0.12
<b>40</b>	<b>120</b>	3.72	3.85	3.95	0.12
	<b>135</b>	3.44	3.36	3.54	0.09
	<b>150</b>	3.23	3.47	3.37	0.12

Table 6.3: Standard deviation of the width of the lines as a function of the arc current.

Speed (mm/min)	$\sigma$ (mm)
120	0.49
135	0.29
150	0.31

Table 6.4: Standard deviation of the height of the lines as a function of the arc current.

Current (Ampere)	$\sigma$ ( mm )
30	0.14
32.5	0.40
35	0.49
37.5	0.35
40	0.42

Table 6.5: Standard deviation of the width of the lines as a function of the printing speed.

Speed (mm/min)	$\sigma$ ( mm )
120	0.13
135	0.13
150	0.12

Table 6.6: Standard deviation of the height of the lines as a function of the printing speed.

Current (Ampere)	$\sigma$ ( mm )
30	0.14
32.5	0.12
35	0.10
37.5	0.16
40	0.11

### 6.3: MACROSCOPICAL ANALYSIS

After mounting, the specimens were grinded, polished, and etched for further light microscopy analysis. Since not all the lines could be detached from the substrate, only 3 lines printed under the same condition were analyzed. It was found that the microstructure of the printed considerably different than that of the as-received material. Under 1000X magnification, a high density of well-dispersed second phase particles can be seen. This microstructure is repeated for all the printed lines regardless the printing parameters or its number within the same printing plate. Both longitudinal and transversal directions show the same arrangement. Figure 6.6 shows a representative microscopy of a printed line. XRD analysis of representative lines indicates the presence of  $\text{Al}_5\text{Mg}_{11}\text{Zn}_4$  precipitate ( $\varphi$  phase) embedded on a Mg matrix ( $\alpha$  phase) (Figure 6.7).

Respecting the defects present within the lines, it was found that the central portion of the lines do not present any void or cavity. However, this is not the case for the periphery sections. Micro-cracks can be found growing from the surface of the lines inwards. However, no crack grows longer than  $288\mu\text{m}$  inside the lines. The majority of these defects can be found in the bottom and the top sections of the printed line. A few internal cracks were detected at distances no larger than  $130\mu\text{m}$  from the surface of the line. Figure 6.7 shows different defects detected on the printed samples. In 6.7A and 6.7B cracks growing from the upper section of the specimen

inwards are shown. This type of defects is present in every line printed. It is believed that it would be possible the elimination of these defects by increasing the flow of shielding gas. However, the equipment used is unable to supply larger amounts than the used. Cracks coming from the bottom of the lines can also be seen on 6.7C and 6.7D. In this case, the cracks are larger than those formed on the top section. There are two different causes for these defects. On 6.7C the reason was a re-melting of the material. 6.7D present a crack formed by large temperature gradients.

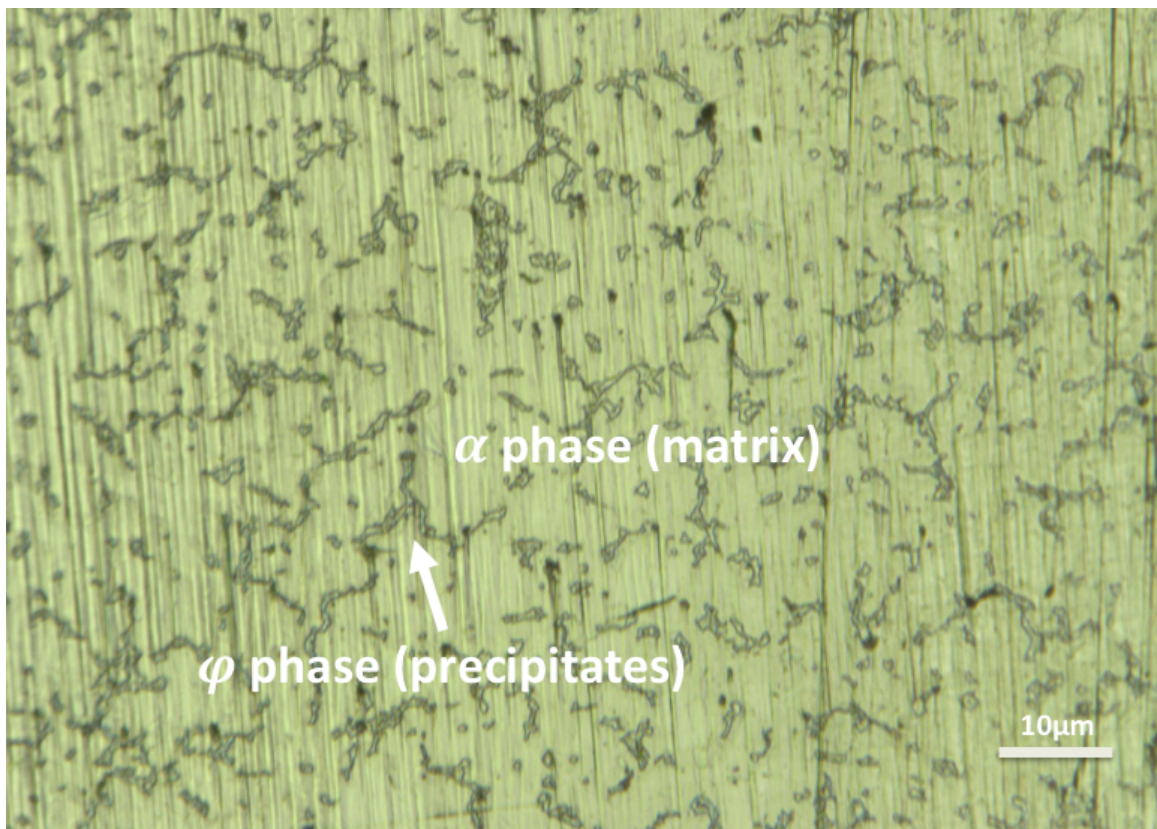


Figure6.6: Representative microstructure of printed lines. Al<sub>5</sub>Mg<sub>11</sub>Zn<sub>4</sub> precipitate ( $\phi$  phase) embedded on a Mg matrix ( $\alpha$  phase). 1000X. Glycol as etchant.



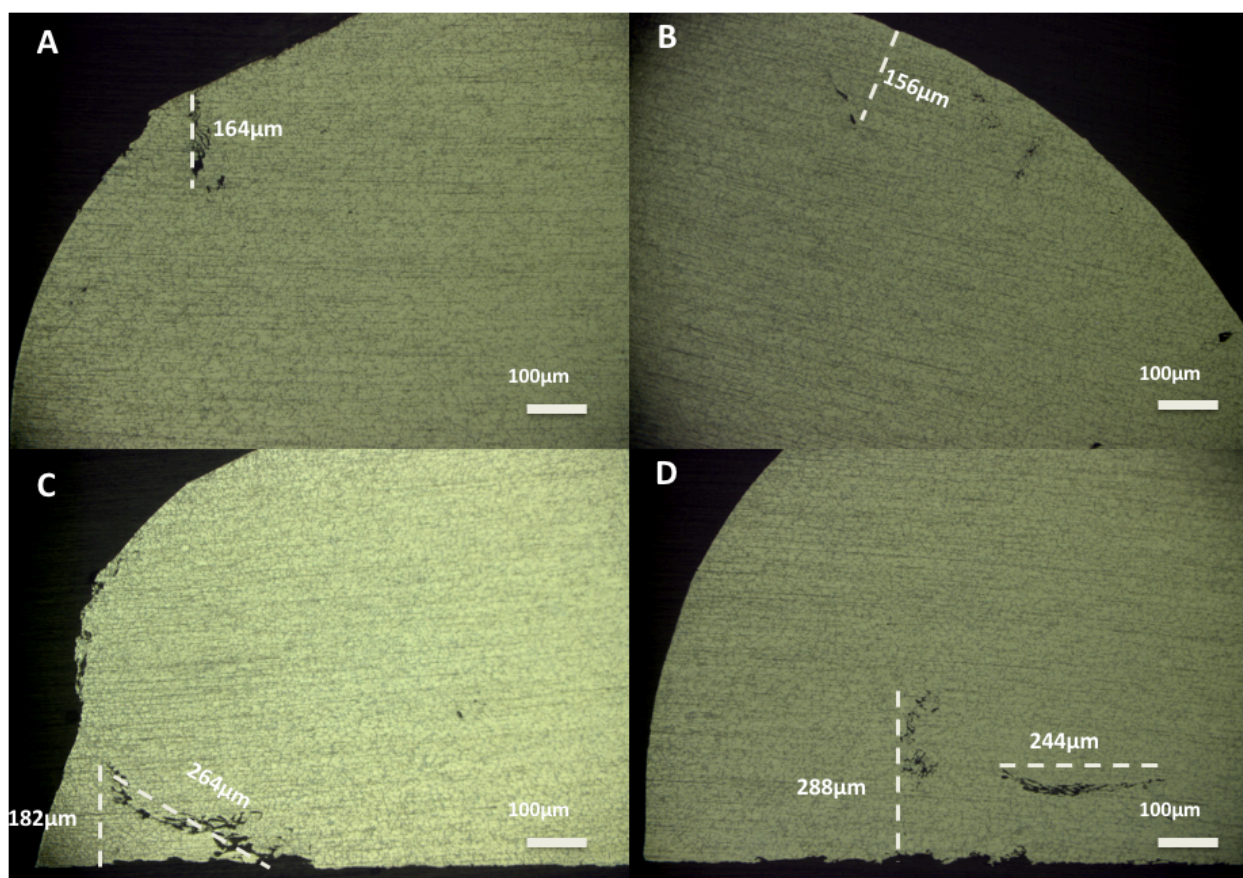


Figure 6.7: Characteristic defects present on printed lines. A&B show cracks formed at the top section of the samples. C&D presenting cracks growing from the bottom inwards

Depending on the heat conditions introduced to the substrate, the morphology of the lines changes. This variation is appreciable on the angle formed by the substrate (bottom section of the line) and the printed line. As the temperature conditions increased, the angle formed (from now called  $\theta$ ) decreased. Figure 6.8 represents the tendency of change as a consequence of the printing conditions. Moreover, the contact angle also changes as a consequence of the temperature of the printing bed at the moment of the printing. As illustrated in Figure 6.4, the temperature of the substrate increases as the number of lines printed on the bed increases. Hence, the contact angle of the line will progressively decrease as more lines are being created. Figure 6.9 presents the change in contact angle as the number of printed lines increases.

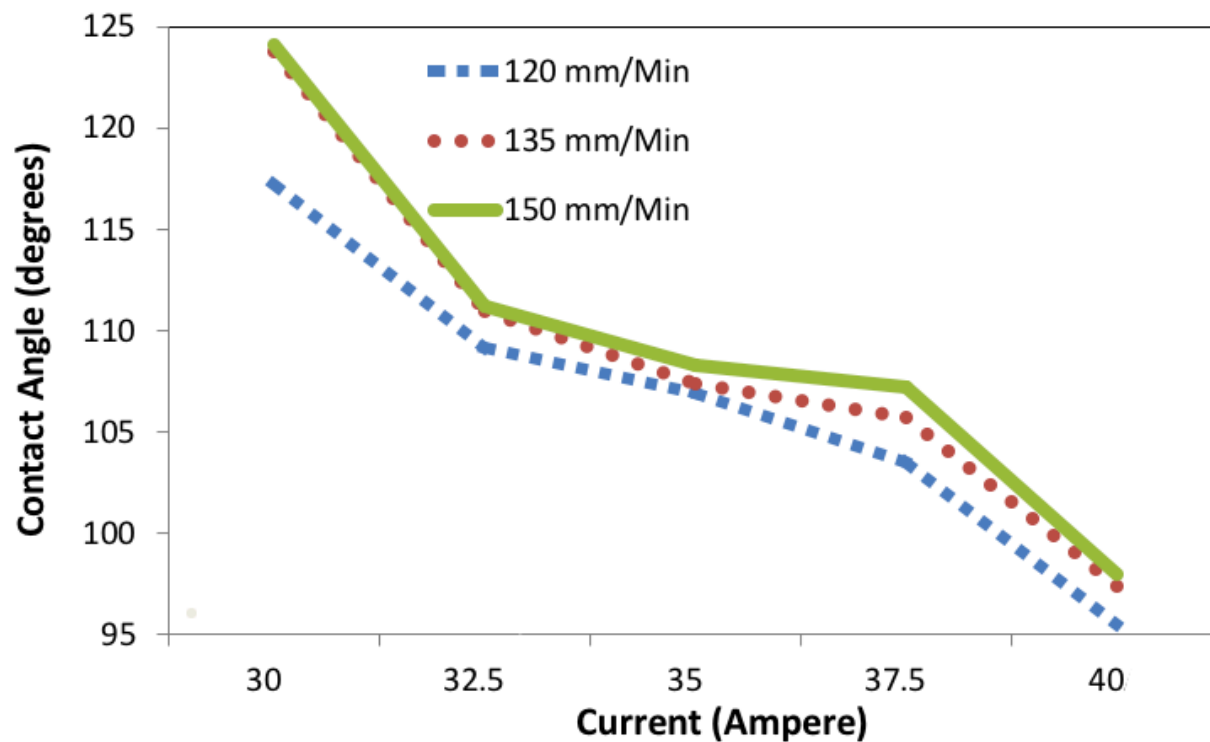


Figure 6.8: Decrease on contact angle (Y axis) as consequence of both printing parameters current intensity (X axis) and printing speed (graphed lines).

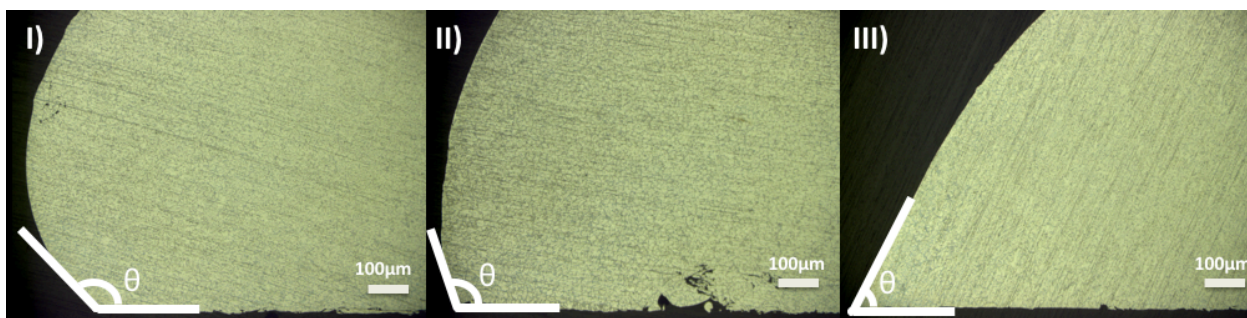


Figure 6.9: Micrographs of lines printed consecutively over the same substrate under the same printing conditions. I) First line printed, II) second line printed, and III) third line printed. The decrease in contact angle as the number of lines printed increases is noticeable.

#### 6.4: DIFFRACTOMETRY AND SPECTROMETRY

XRD results show that the printed specimens are composed by a mixture of Al<sub>5</sub>Mg<sub>11</sub>Zn<sub>4</sub> precipitates ( $\phi$  phase) and a magnesium matrix ( $\alpha$  phase), as can be seen on Figure 6.10. It is noticeable that the characteristic peaks are shifted to the left-hand side (lower angle). The shifting could be created by compressive stresses introduced to the specimen during the printing process.

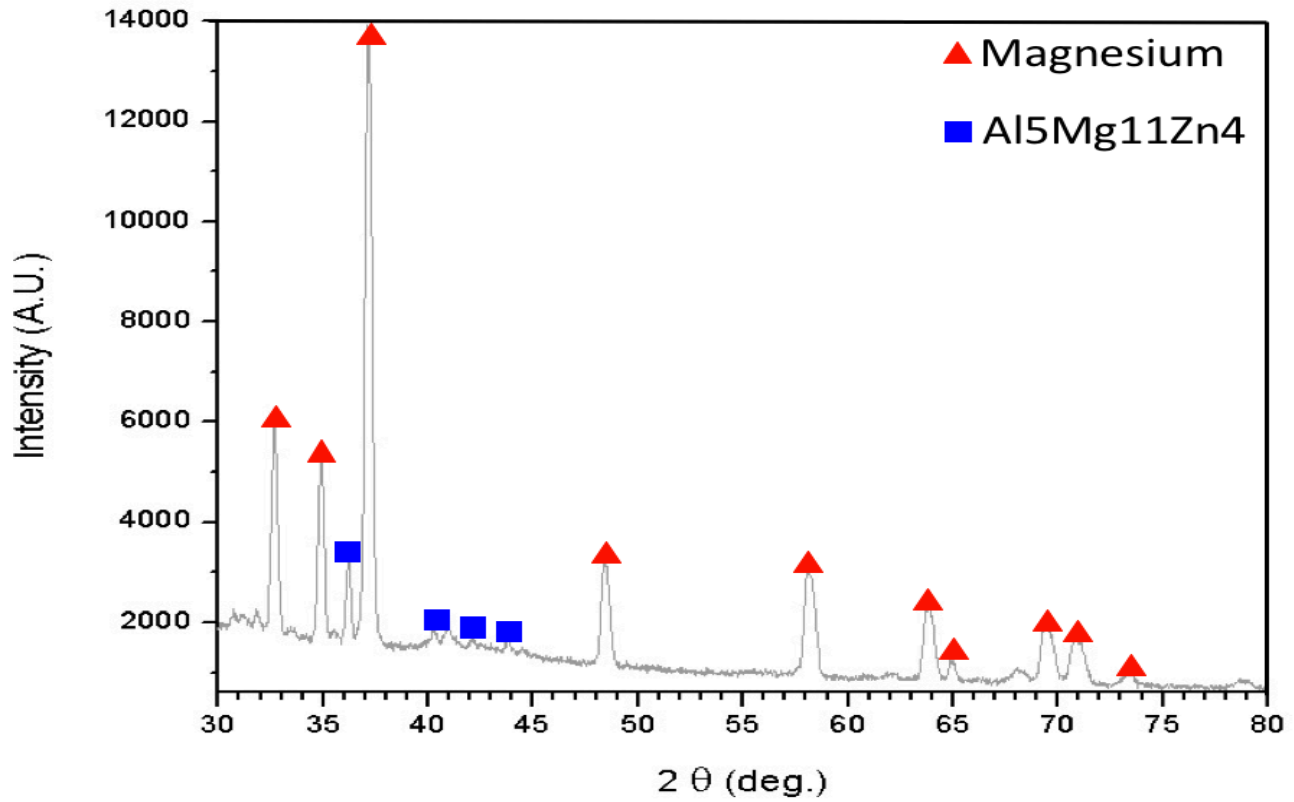


Figure 6.10: XRD spectra of a representative printed line. Representative peaks of pure magnesium ( $\alpha$  phase) and Al<sub>5</sub>Mg<sub>11</sub>Zn<sub>4</sub> precipitates ( $\phi$  phase).

Elemental mapping of two different sections of a representative specimen was gotten with the use of EDS. Illustration 6.1 schematically shows the areas in which this analysis was performed. As shown in Table 5.1, the most abundant elements in the alloy are magnesium, aluminum, and zinc. SEM images were contrasted with the elemental mapping obtained by the use of EDS in order to determine where the chemical elements are located within the cross-section area of the lines, as shown in Figure 6.11 and 6.12. The higher concentration of aluminum and zinc can be found inside the  $\phi$  phase precipitates, along the grain boundaries.

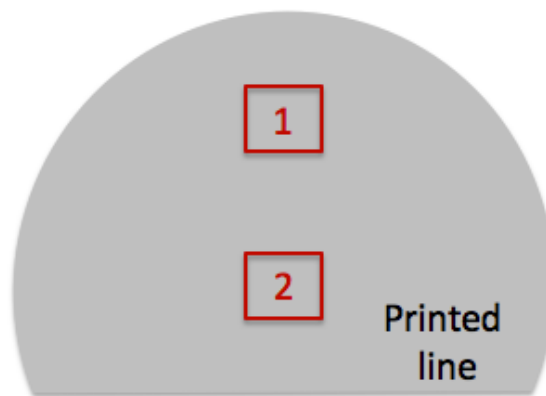


Illustration 6.1: Diagram representing the areas from which the elemental mappings were gotten.



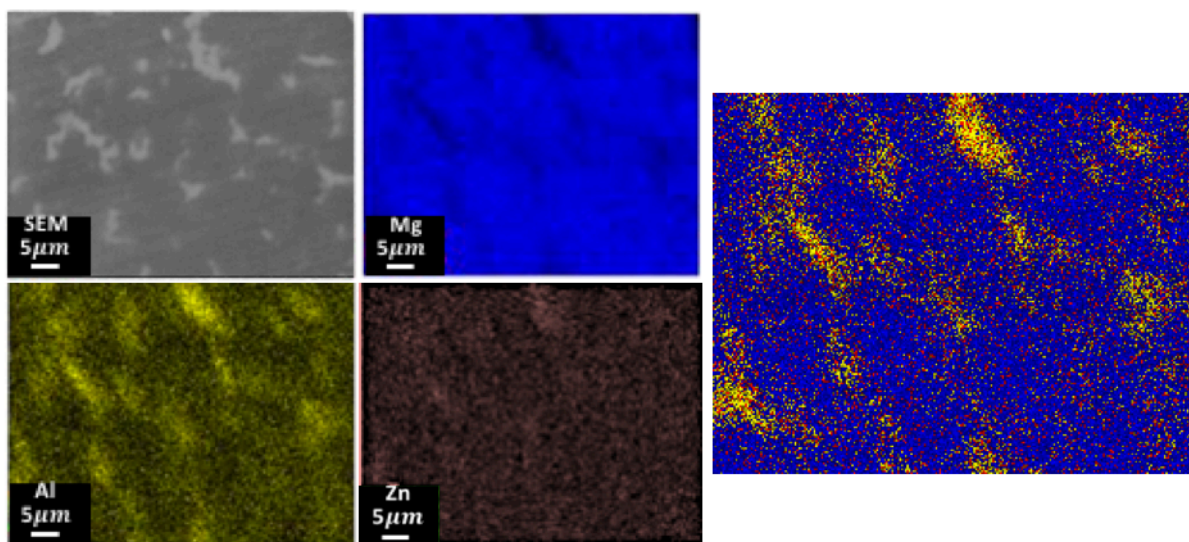


Figure 6.11: Elemental Mapping of zone 1.

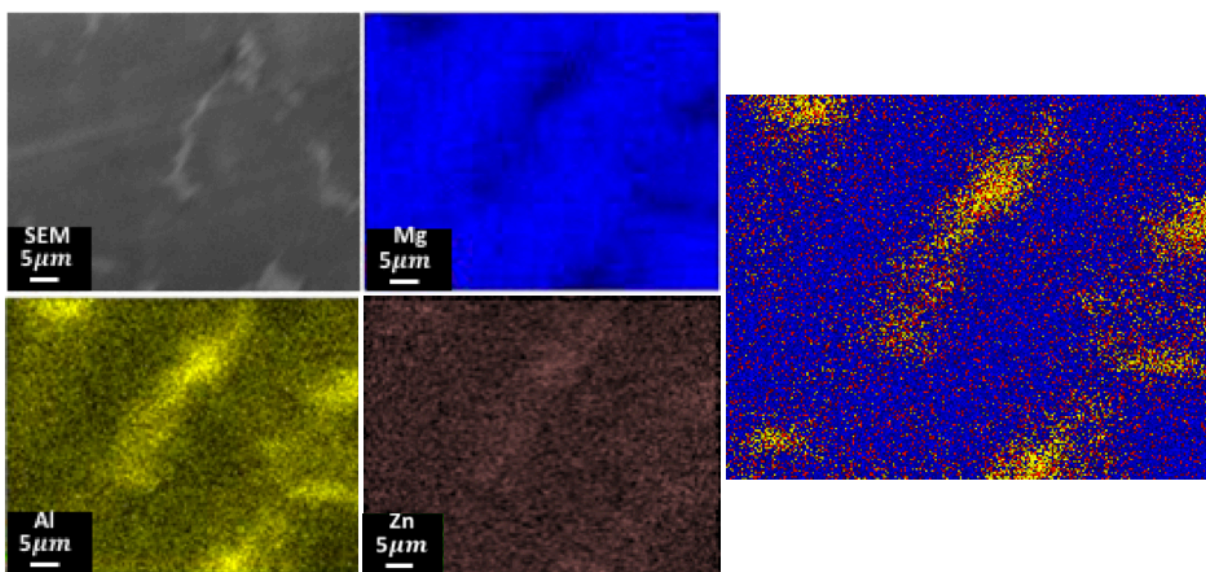


Figure 6.12: Elemental Mapping of zone 2.

## 6.5: CHARACTERIZATION OF BY-PRODUCTS

During the printing process, two different by-products are created depending on the printing conditions. When using printing parameters that introduce low heat to the system, a black stain covers the areas adjacent to the printed line. A spatula can be used to remove the stain, which is actually a fine powder. As the temperature increases, a white powder evolves in the areas previously covered by the black powder. Usually, a combination of these two products is found surrounding the specimens, being predominant the presence of the black powder in almost all the cases. However, when 40A is used as arc current, the white powder is predominant. Figure 7.10 shows lines presenting different powders. 6.13A was printed under low heat conditions, while 6.13B was created under high heat conditions. By analyzing both by-products with XRD it was discovered that the black powder is pure magnesium particles, while the white powder is magnesium oxide. An XRD spectrum of a mixture of powders is shown in Figure 6.14.

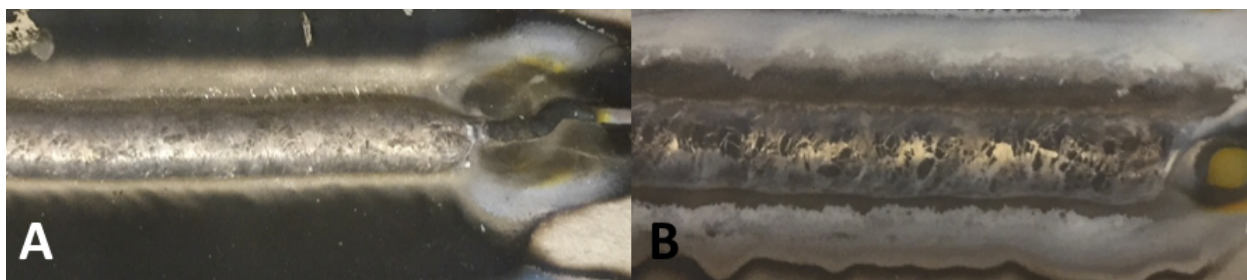


Figure 6.13: Different by-products created depending on printing conditions. 6.12A; line printed under low heat conditions presenting black powder. 6.12B; Line printed using higher heat input presenting white a mixture of white and black powder.

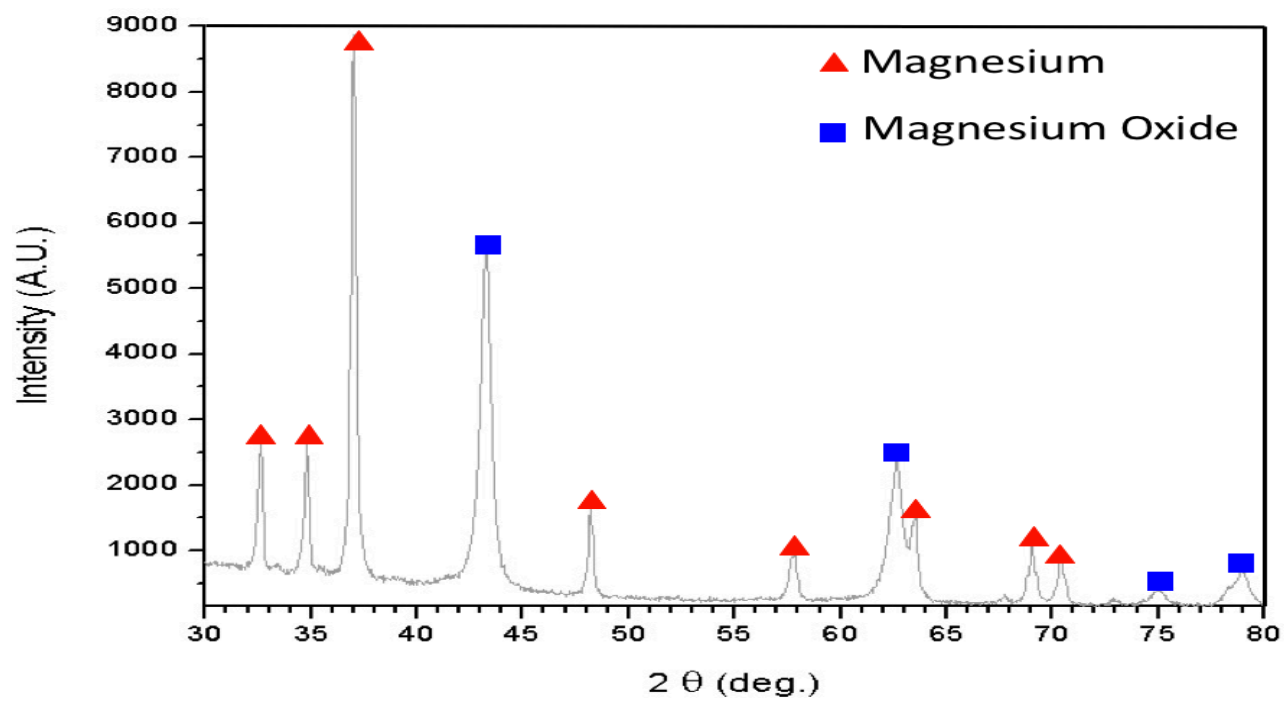


Figure6.14: XRD spectra of by-products. Pure magnesium (black powder) and magnesium oxide (white powder) were found.

## Chapter 7: Discussion

### 7.1: ON MACROSCOPICAL APPEARANCE

For pure metals, and the majority of the alloys, surface tension decreases as temperature increases. Since the surface tension is temperature dependent, gradients will exist on a weld pool. When a surface tension gradient exists, the liquid will be drawn-along to those regions of higher surface tension. In some cases, the force generated by the surface tension gradient can be large enough to dominate other forces present in the liquid. Thus, the areas with lowest temperatures (solidified sections) will drag the molten metal[59]. This phenomenon can be observed on those lines printed under conditions where high currents were used (high heat input). In the case of condition D (high current and high speed), the molten metal was dragged by that first section printed. Since the printing plate was first at room temperature, more heat was able to be withdrawn from the welding line at the beginning of the process. A thermal gradient was created between the starting point and the advancing printing front. Figure 7.1 shows the line printed under condition D. It is observable how the first and last sections of the welding line are connected by a thin line. It can be visualized as a “river” through which the molten metal was drawn along to the beginning specimen. Similarly, conditions E (high current and moderately high speed) yield a thick but partitioned line. A temperature gradient was first created, however, since the printing speed was lower than that of condition D, more time was available to reach thermal equilibrium. Hence, the material was able to distribute in a more homogeneous manner. From this reasoning we can conclude that the best printing conditions are those in which the temperature gradient created is the lowest possible in order to form uniform specimens.

The dimensions of the printed lines presented large standard deviation. Tables 6.1 and 6.2 show the average thickness and width of the first, second and third line printed on the same substrate under the same printing conditions respectively. Tables 6.3, 6.4, 6.5, and 6.6 show the standard deviation of the measurements in both dimensions as a function of the printing speed and arc current. No correlation between the printing conditions and the change in dimensions



was found. It is known that the coefficient of thermal expansion of magnesium alloys (Table 5.2) is even higher of that of aluminum. This would represent a difficulty at the moment of welding magnesium alloys, since large deformations are expected. High thermal conductivity would also be a reason of the uneven dimensions[41]. Since heat can be conducted away from the heat more rapidly, thermal gradients can be easily formed. Consequently, the drag-along effect can be a cause of the dimensional irregularity. In order to solve this problem, a precise control over the temperature in the system must be attained. However, due to the constant introduction of heat through the arc into the system makes this task hard to achieve.

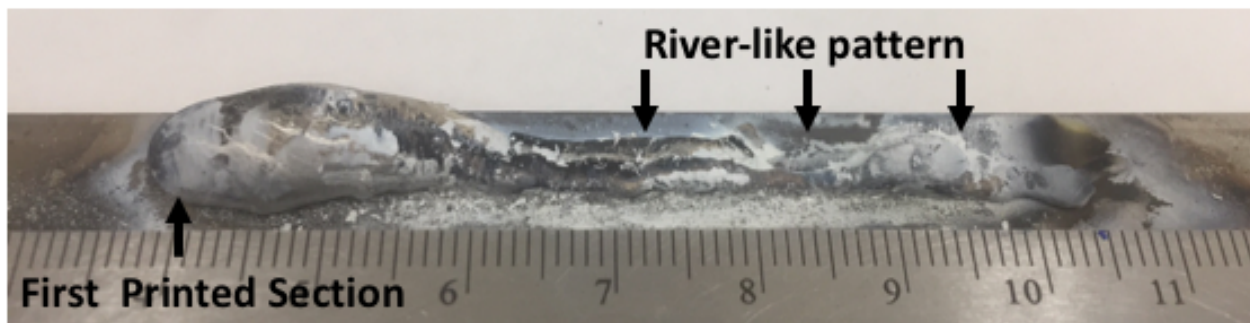


Figure 7.1: Line printed under conditions of high heat and high speed. A “river-like pattern”, through which the molten metal flowed while dragged along the solidified metal (beginning on the line).

## 7.2: ON CONTACT ANGLE

In the bulk of any solid or liquid, the net forces of the atoms are relatively small. This because the surrounding atoms exert forces in all direction, thus, there is a little or no resultant. For those atoms on the surface, there is a resultant attraction inwards since the molecular density in the liquid is much larger than that of the vapor. Thus, the liquid will try to contract as much as possible, becoming a sphere. The tendency of the surface atoms to contract can be considered a state of tension, hence the name surface tension. When dealing with solids the behavior will be the same as in liquids. In this case, however, the term surface energy is more appropriate. When

three immiscible phases are in contact, the angle of their interfaces at the point of contact are such that their interfacial forces (forces required to extend the interface between a solid and a liquid) are balanced out. Illustration 7.1 shows a diagram of a liquid drop placed on a flat solid surface. The same model can be used to describe the morphology of the printed lines. However, in the case of the printed lines many conditions may affect the shape of the final product. The most important factors that would change the form of the specimens are [60]:

- a) The width of the weld pool.
- b) The volume of metal added to the weld pool.
- c) The hydrostatic pressure in the molten wire bead.
- d) The velocity with which metal flows towards the rear end to the weld pool.

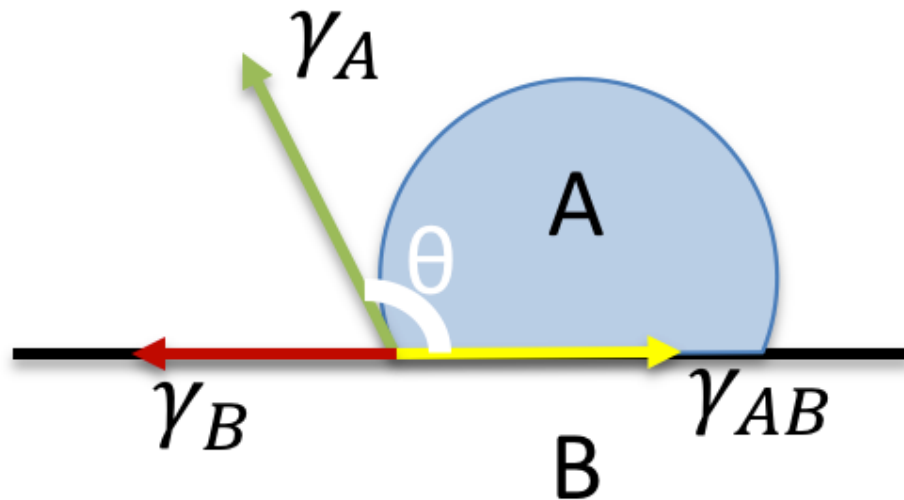


Illustration 7.1: Forces involved in the determination of the contact angle of a liquid drop over a flat solid surface.

In this study, a decrement in the contact angle as a function of the heat conditions was detected. For all the printing parameters the wire feed rate remained constant. The flow rate of both the pilot arc and the shielding gas was also kept constant. Thus, only two out of the four

parameters affecting the contact angle of the printed specimens were varied. First, the size of the weld pool which is in direct correlation with the current intensity. As the supplied current increases, more heat is delivered to the substrate and, as a consequence, the size of the molten pool increases. The velocity with which metal flows towards the rear end to the weld pool can be interpreted as the printing speed since, in order to get uniform lines, the arc must follow the wire all the time (Illustration 4.5). Figure 6.8 shows how by increasing the size of the molten pool (increasing current) the contact angle would decrease since the surface energy differential between the molten substrate and the depositing metal would be lower than that between a solid substrate and a liquid filler. Table 7.1 shows the heat input into the system depending on the printing conditions. Noticeable is the fact that the amount of heat delivered into the system is directly proportional to the arc current and inversely proportional to the printing speed. To calculate the heat input the following formula was used:

$$Heat\ Input = \frac{Arc\ Voltage * Arc\ Current * Thermal\ Efficiency}{Travel\ speed}$$

where arc voltage is 25 volts (constant for all the cases), thermal efficiency is 60% for PAW, and arc current (Ampere) and travel speed (mm/sec) are variables [50].

Table 7.1: Heat input depending on printing conditions.

Current (Ampere)	Printing Speed (mm/min)	Heat Input (kJ/mm)
30	120	0.225
30	135	0.200
30	150	0.180
32.5	120	0.244
32.5	135	0.217
32.5	150	0.195
35	120	0.263
35	135	0.233
35	150	0.210
37.5	120	0.281
37.5	135	0.250
37.5	150	0.225
40	120	0.300
40	135	0.267
40	150	0.240

Due to the relatively low melting point of magnesium and its alloys, re-melting is a common problem when welding these materials [41]. Thus, as the temperature of the substrate increases as a consequence of the increasing number of lines printed over the same plate, the lines become more susceptible to re-melting. It is believed that, along the increased size of the molten pool, re-melting is a cause of the reduction of contact angle between the substrate and the printed line as more lines are printed over the same plate. Figure 7.3 shows two examples of lines presenting re-melting. It is noticeable a dramatic change in contact angle on the areas closest to the substrate. This indicates that heat coming from the printing plate was enough to melt part of the printed line.

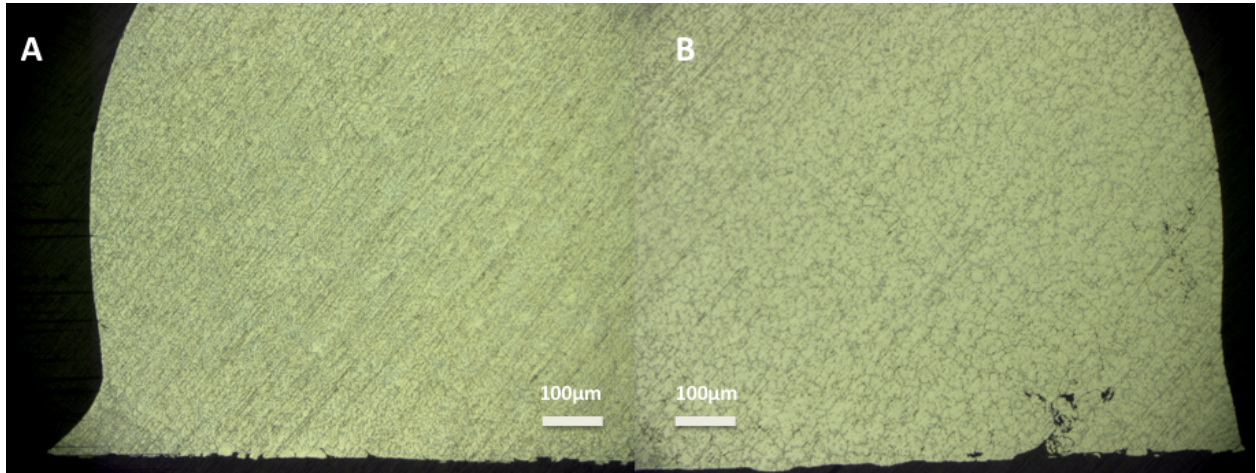


Figure 7.3: Micrographs of two printed lines presenting a decrease in the contact angle due to re-melting.

### 7.3: ON MICROSTRUCTURAL CHANGES

XRD indicates that two phases are present in the specimens. Al<sub>5</sub>Mg<sub>11</sub>Zn<sub>4</sub> supersaturated solid solution ( $\phi$ ), with an orthorhombic crystal structure precipitated along the grain boundaries. It is observable that the representative peaks of the hexagonal Mg are right-shifted, indicating either a stoichiometry change or compressive stress in the specimen. The presence of internal stresses is a consequence of the large difference in lattice parameters between the HCP magnesium matrix ( $a=3.2\text{ \AA}$ ,  $b=3.2\text{ \AA}$ , and  $c=5.2\text{ \AA}$ ) and the orthorhombic  $\phi$  phase ( $a=9\text{ \AA}$ ,  $b=17\text{ \AA}$ , and  $c=19.7\text{ \AA}$ ). By comparing the microstructure present in the printed lines, a discussion about the presence Al<sub>5</sub>Mg<sub>11</sub>Zn<sub>4</sub> precipitate is called into question. Many researchers indicate that  $\phi$  phase precipitates in alloys with high concentration of zinc (>8%wt) and low aluminum content (4wt%)[61]. The most commonly accepted second phase particles present in AZ91D are Mg<sub>17</sub>Al<sub>12</sub> ( $\beta$ ), which also precipitate along the grain boundaries, increasing the corrosion and creep resistance of the alloy[62], [63]. However, high concentration of zinc along the grain boundaries shown on the EDS mappings (Figure 6.11 & 6.12) indicates that the precipitates are indeed  $\phi$  phase precipitates.

## Chapter 8: Conclusions

In this research, it has been proved that magnesium alloy AZ91D can be used for the creation of specimens using WAAM systems. In order to obtain uniform base lines, the thermal gradient generated by the plasma arc has to be reduced by controlling the movement of the printing bed. The high thermal expansion coefficient of magnesium affects the uniformity on the dimensions of both width and height of the printed lines. No correlation whatsoever has been found between any printing parameter and the dispersion of measurements of the samples. Besides the large expansion coefficient, differences in surface energy between the molten pool and the unaffected substrate produced by the arc influence the uniformity of the lines. The “drag-along” effect, consequence of thermal gradients that generate changes in surface energy create undesired agglomeration of metal in those areas where the molten material solidified first. Thus, in order to print visually uniform lines, it is important to reduce the thermal gradients. This can be achieved by finding equilibrium between the heat supplied by the arc (current) and the printing speed.

It was noticed that the contact angle between the printed specimen and the substrate decreases as the heat conditions increases. This is a consequence of the size of molten pool. As more current is used, the diameter of the molten pool will be bigger. Thus, the difference in surface energy of both the substrate and the filler material is reduced, and the line would “spread” easily over the printing plate. Also, as the number of printed lines over the same substrate increments, the angle contact angle of these consecutive lines also decreases. In this case, the reason of the decrement is the re-melting of those areas close to the substrate due to the combination of heat coming out of the plate and the heat irradiated by the arc. Hence, the morphology of the printed lines could be tailored by controlling the temperature present in the system during the fabrication process.

The finally, the orthorhombic phase present in the microstructure is not what is expected for this alloy. Aided by the high thermal conductivity coefficient, shielding gas stream required

for the removal of air during the welding process propitiated a rapid cooling rate (air-quench). Since diffusion was rapidly stopped, zinc atoms were not allowed to migrate from the grain boundaries into the bulk crystals. Thus,  $\text{Al}_5\text{Mg}_{11}\text{Zn}_4$  precipitate was then formed.

## References

- [1] W. E. Frazier, "Metal additive manufacturing: A review," *J. Mater. Eng. Perform.*, vol. 23, no. 6, pp. 1917–1928, 2014.
- [2] D. Ding, Z. Pan, D. Cuiuri, and H. Li, "Wire-feed additive manufacturing of metal components: technologies, developments and future interests," *Int. J. Adv. Manuf. Technol.*, vol. 81, no. 1–4, pp. 465–481, 2015.
- [3] "Electron Beam Melting," 2017. [Online]. Available: <https://additivemanufacturingllc.com>.
- [4] N. P. Kim, J.-S. Eo, and D. Cho, "Optimization of piston type extrusion (PTE) techniques for 3D printed food," *J. Food Eng.*, vol. 235, pp. 41–49, 2018.
- [5] N.-S. Kim and K. N. Han, "Future direction of direct writing," *J. Appl. Phys.*, vol. 108, no. 10, p. 102801, 2010.
- [6] K. N. Han and N. S. Kim, "Challenges and opportunities in direct write technology using nano-metal particles," *KONA Powder Part. J.*, vol. 27, no. 27, pp. 73–83, 2009.
- [7] S. Hong and N. Kim, "Synthesis of 3D Printable Cu???Ag Core???Shell Materials: Kinetics of CuO Film Removal," *J. Electron. Mater.*, vol. 44, no. 3, pp. 823–830, 2015.
- [8] W. Aiyiti, W. Zhao, B. Lu, and Y. Tang, "Investigation of the overlapping parameters of MPAW-based rapid prototyping," *Rapid Prototyp. J.*, vol. 12, no. 3, pp. 165–172, 2006.
- [9] D. D. Gu, W. Meiners, K. Wissenbach, and R. Poprawe, "Laser additive manufacturing of metallic components: materials, processes and mechanisms," *Int. Mater. Rev.*, vol. 57, no. 3, pp. 133–164, 2012.
- [10] K. V. Wong and A. Hernandez, "A Review of Additive Manufacturing," *ISRN Mech. Eng.*, vol. 2012, pp. 1–10, 2012.
- [11] G. H. Wu and S. H. Hsu, "Review: Polymeric-based 3D printing for tissue engineering," *J. Med. Biol. Eng.*, vol. 35, no. 3, pp. 285–292, 2015.
- [12] A. T. Sidambe, "Biocompatibility of advanced manufactured titanium implants-A review," *Materials (Basel)*, vol. 7, no. 12, pp. 8168–8188, 2014.
- [13] L. E. Murr *et al.*, "Metal Fabrication by Additive Manufacturing Using Laser and Electron Beam Melting Technologies," *J. Mater. Sci. Technol.*, vol. 28, no. 1, pp. 1–14, 2012.
- [14] J. Kruth, B. Vandenbroucke, J. Vaerenbergh, and P. Mercelis, "Benchmarking of different SLS/SLM processes as rapid manufacturing techniques," *Int. Conf. Polym. Mould. Innov. (PMI), Gent, Belgium, April 20-23, 2005*, pp. 1–7, 2005.
- [15] "3D printing VS CNC." [Online]. Available: source: <http://www.stratasys.com/resources/search/white-papers/3d-printing-vs-cnc>.
- [16] Č. Jaroslav and D. Vojtěch, "Characterization of porous magnesium prepared by powder metallurgy - influence of powder shape," *Manuf. Technol.*, vol. 14, no. 3, pp. 271–275, 2014.



- [17] G. Egger, P. E. Gygax, R. Glardon, and N. P. Karapatis, "Optimization of powder layer density in selective laser sintering," *10th Solid Free. Fabr. Symp.*, pp. 255–263, 1999.
- [18] A. K. Amert, D. H. Oh, and N. S. Kim, "A simulation and experimental study on packing of nanoinks to attain better conductivity," *J. Appl. Phys.*, vol. 108, no. 10, 2010.
- [19] K. N. Amato, S. M. Gaytan, L. E. Murr, E. Martinez, and P. W. Shindo, "Microstructures and mechanical behavior of Inconel 718 fabricated by selective laser melting," *Acta Mater.*, vol. 60, no. 5, pp. 2229–2239, 2012.
- [20] J. L. Hall, "Cellular mechanisms for heavy metal detoxification and tolerance," *J. Exp. Bot.*, vol. 53, no. 366, pp. 1–11, 2002.
- [21] L. Liu, G. Song, G. Liang, and J. Wang, "Pore formation during hybrid laser-tungsten inert gas arc welding of magnesium alloy AZ31B — mechanism and remedy," 2004.
- [22] F. Wang, S. Williams, P. Colegrove, and A. A. Antonysamy, "Microstructure and mechanical properties of wire and arc additive manufactured Ti-6Al-4V," *Metall. Mater. Trans. A Phys. Metall. Mater. Sci.*, vol. 44, no. 2, pp. 968–977, 2013.
- [23] J. P. Kruth, X. Wang, T. Laoui, and L. Froyen, "Lasers and materials in selective laser sintering," *Assem. Autom.*, vol. 23, no. 4, pp. 357–371, 2003.
- [24] S. W. Williams, F. Martina, A. C. Addison, J. Ding, G. Pardal, and P. Colegrove, "Wire + Arc Additive Manufacturing," *Mater. Sci. Technol.*, vol. 32, no. 7, pp. 641–647, 2016.
- [25] W. Tang and A. P. Reynolds, "Production of wire via friction extrusion of aluminum alloy machining chips," *J. Mater. Process. Technol.*, vol. 210, no. 15, pp. 2231–2237, 2010.
- [26] A. Milenin and P. Kustra, "Numerical and experimental analysis of wire drawing for hardly deformable biocompatible magnesium alloys," *Arch. Metall. Mater.*, vol. 58, no. 1, pp. 55–62, 2013.
- [27] H. Kennet, *Fundamentals of Aqueous Metallurgy*. SME, 2002.
- [28] K. Taminger and R. Hafley, "Electron beam freeform fabrication: a rapid metal deposition process," *Proc. 3rd Annu. Automot. Compos. Conf.*, pp. 9–10, 2003.
- [29] S. Ramakrishna, J. Mayer, E. Wintermantel, and K. W. Leong, "Biomedical applications of polymer-composite materials : a review," vol. 61, 2001.
- [30] K. Rezwan, Q. Z. Chen, J. J. Blaker, and A. R. Boccaccini, "Biodegradable and bioactive porous polymer/inorganic composite scaffolds for bone tissue engineering," *Biomaterials*, vol. 27, no. 18, pp. 3413–3431, 2006.
- [31] M. Niinomi, "Recent metallic materials for biomedical applications," *Metall. Mater. Trans. A*, vol. 33, no. 3, pp. 477–486, 2002.
- [32] M. I. Z. Ridzwan, S. Shuib, A. Y. Hassan, A. A. Shokri, and M. N. Mohammad Ibrahim, "Problem of stress shielding and improvement to the hip implant designs: A review," *Journal of Medical Sciences*, vol. 7, no. 3, pp. 460–467, 2007.
- [33] C. Lhotka, T. Szekeres, I. Steffan, K. Zhuber, and K. Zweymüller, "Four-year study of cobalt and chromium blood levels in patients managed with two different metal-on-metal total hip replacements.," *J. Orthop. Res.*, vol. 21, no. 2, pp. 189–95, 2003.

- [34] Y. Park, JB Kim, “Metallic biomaterials,” in *Biomaterials principles and applications*, Boca Raton, 2003.
- [35] M. P. Staiger, A. M. Pietak, J. Huadmai, and G. Dias, “Magnesium and its alloys as orthopedic biomaterials: A review,” *Biomaterials*, vol. 27, no. 9, pp. 1728–1734, 2006.
- [36] F. Witte and A. Eliezer, “Biodegradable metals,” *Degrad. Implant Mater.*, vol. 9781461439, pp. 93–109, 2012.
- [37] N. Li and Y. Zheng, “Novel Magnesium Alloys Developed for Biomedical Application: A Review,” *J. Mater. Sci. Technol.*, vol. 29, no. 6, pp. 489–502, 2013.
- [38] F. Witte *et al.*, “In vitro and in vivo corrosion measurements of magnesium alloys,” vol. 27, pp. 1013–1018, 2006.
- [39] F. Witte *et al.*, “Degradable biomaterials based on magnesium corrosion,” *Curr. Opin. Solid State Mater. Sci.*, vol. 12, no. 5–6, pp. 63–72, 2008.
- [40] X. Cao, M. Jahazi, J. P. Immarigeon, and W. Wallace, “A review of laser welding techniques for magnesium alloys,” vol. 171, pp. 188–204, 2006.
- [41] E. G. West, *The Welding of Non-Ferrous Metals*, First. New York: John Wiley & Sons, 1951.
- [42] J. A. Esparza, W. C. Davis, E. A. Trillo, and L. E. Murr, “Friction-stir welding of magnesium alloy AZ31B,” pp. 917–920, 2002.
- [43] “TIG Welding Magnesium.” .
- [44] “RepRap.” [Online]. Available: <http://www.reprap.cc/shop/en/content/ramps-14>. [Accessed: 21-Mar-2018].
- [45] M. P. Groover, *Fundamentals of Modern Manufacturing*, Fifth. .
- [46] S. Kou, *Welding Metallurgy*, Second. 2003.
- [47] G. Linnert, *Welding Metallurgy*, Fourth. GML Publications.
- [48] “TIG VS PAW.”
- [49] “AZ91D,” *DYNACAST*, 2018. [Online]. Available: <https://www.dynacast.com/az91d>. [Accessed: 11-Apr-2018].
- [50] H. Huo, Y. Li, and F. Wang, “Corrosion of AZ91D magnesium alloy with a chemical conversion coating and electroless nickel layer,” *Corros. Sci.*, vol. 46, no. 6, pp. 1467–1477, 2004.
- [51] F. Seuss, S. Seuss, M. C. Turhan, B. Fabry, and S. Virtanen, “Corrosion of Mg alloy AZ91D in the presence of living cells,” *J. Biomed. Mater. Res. - Part B Appl. Biomater.*, vol. 99 B, no. 2, pp. 276–281, 2011.
- [52] R. W. Chan, Ed., *Materials Science and Technology A Comprehensive Treatment*, The Classi. Wiley-vch, 2005.
- [53] N. E. Woldman, *Engineering Alloys; names, properties, uses.*, 3rd ed. American Society of Materials, 1954.
- [54] D. Cohen, “Stainless Steel - Grade 316 (UNS S31600),” 2018. [Online]. Available:

- <https://www.azom.com/article.aspx?articleid=863>. [Accessed: 12-Apr-2018].
- [55] B. George and V. Voort, “Metallography of Magnesium and its Alloys,” *Tech Notes*, vol. 4, no. 2, pp. 1–5, 2015.
  - [56] Y. Leng, *Materials Characterization: Introduction to Microscopic and Spectroscopic Methods*, First. John Wiley & Sons (Asia), 2008.
  - [57] “The D8 Family.” [Online]. Available: <https://www.bruker.com/products/x-ray-diffraction-and-elemental-analysis/x-ray-diffraction/d8-advance/overview.html>. [Accessed: 15-Mar-2018].
  - [58] F. J. Humpherys, *Recrystallization and Related Annealing Phenomena*, First. Elsevier B.V, 2012.
  - [59] F. Wang, *Materials Processing Theory And Practices*, 8th ed. 1990.
  - [60] J. F. Lancaster, *The Physics of Welding*, First. Pergamon Press, 1984.
  - [61] M. Youping, W. Weixin, L. Pengfei, and X. Kewei, “Effects of Treatment Parameters on Microstructure of Diffusion Alloyed Coatings on Pure Magnesium.,” *Surf. Eng.*, vol. 20, no. 2, pp. 108–112, 2004.
  - [62] D. G. L. Prakash and D. Regener, “Quantitative characterization of Mg<sub>17</sub>Al<sub>12</sub> phase and grain size in HPDC AZ91 magnesium alloy,” *J. Alloys Compd.*, vol. 461, no. 1–2, pp. 139–146, 2008.
  - [63] ASM, *ASM Speciality Handbook Magnesium and Magnesium Alloys*, Second. ASM International, 1999.

## **Vita**

The author of this thesis was born in Delicias, Chihuahua, Mexico, on November 27<sup>th</sup> of 1991. After finishing his high school studies at Preparatoria Federal por Cooperacion Activo 20-30 “Albert Einstein” June 2009, he moved to Chihuahua city to pursuit his first degree. On June 2014 he was awarded with a degree on Civil Engineering from Universidad Autonoma de Chihuahua. On August 2014, the author started his studies at The University of Texas at El Paso, pursuing a degree on Metallurgical and Materials Engineering. He started his career as undergraduate research assistant at the Printable Nano-Engineering (PNE) center on February 2016. On December of the same year, he was awarded with the degree of Bachelor’s in Science on Metallurgical and Materials Engineering. After that, he continued his labor, now as graduate research assistant on the PNE center. The author defended this thesis on May 4<sup>th</sup>, 2018.

Permanent address: Ave. Rio San Pedro Sur #59  
Delicias, Chihuahua, 33086

This thesis was typed by David Adrian Martinez Holguin.